

DELTA: A DAG-aware Efficient OCS Logical Topology Optimization Framework for AIDCs

Nianguen Ye, Jingya Liu, Weiqiang Sun, *Senior Member, IEEE*, and Weisheng Hu, *Member, IEEE*

Abstract—The rapid scaling of large language models (LLMs) exacerbates communication bottlenecks in AI data centers (AIDCs). To overcome this, optical circuit switches (OCS) are increasingly adopted for their superior bandwidth capacity and energy efficiency. However, their reconfiguration overhead precludes intra-iteration topology update, necessitating a priori engineering of a static topology to absorb time-varying LLM traffic. Existing methods engineer these topologies based on traffic matrices. However, this representation obscures the bursty concurrent bandwidth demands dictated by parallelization strategies and fails to account for the independent channels required for concurrent communication.

To address this, we propose DELTA, an efficient logical topology optimization framework for AIDCs that leverages the computation-communication directed acyclic graph (DAG) to encode time-varying traffic patterns into a Mixed-Integer Linear Programming (MILP) model, while exploiting the temporal slack of non-critical tasks to save optical ports without penalizing iteration makespan. By pioneering a variable-length time interval formulation, DELTA significantly reduces the solution space compared to the fixed-time-step formulation. To scale to thousand-GPU clusters, we design a dual-track acceleration strategy that combines search space pruning (reducing complexity from quadratic to linear) with heuristic hot-starting. Evaluations on large-scale LLM workloads show that DELTA reduces communication time by up to 17.5% compared to state-of-the-art traffic-matrix-based baselines. Furthermore, the framework reduces optical port consumption by at least 20%; dynamically reallocating these surplus ports to bandwidth-bottlenecked workloads reduces their performance gap relative to ideal non-blocking electrical networks by up to 26.1%, ultimately enabling most workloads to achieve near-ideal performance.

Index Terms—AI data center, optical circuit switch, logical topology, mixed-integer linear programming.

I. INTRODUCTION

Driven by the vision of Artificial General Intelligence (AGI) and the scaling laws of LLMs [1, 2], AIDCs are undergoing rapid expansion. However, the evolution of computational demand has outpaced the iteration of underlying network equipment, making communication an increasingly prominent bottleneck for cluster scaling [3–7]. Existing multi-tier electrical Clos networks that support massive GPU interconnections struggle to bridge this gap. Specifically, as endpoint GPU communication rates surge, relying exclusively on electrical packet switches (EPS) not only introduces severe bottlenecks in power consumption [6, 8–11] and latency [10–12], but the frequent upgrades to match these endpoint rates also

incur prohibitive infrastructure churn [13–15]. Consequently, the industry is introducing OCS—leveraging their low power, low latency, and data-rate transparency—to replace the EPS in original Core or Spine layers, driving the emergence of OCS-AIDCs that enable efficient inter-Pod optical connectivity while retaining flexible intra-Pod electrical switching [13–18].

However, unlike the flexible any-to-any connectivity of EPS, the coarse-grained, point-to-point nature of OCS struggles to accommodate the dynamic communication patterns in LLM training. Furthermore, while an OCS can reconfigure optical circuits within tens of milliseconds [14, 15, 19], the subsequent initialization of associated components—such as transceivers, NICs, and EPSs (update the routing tables in order)—requires several seconds [19–21]. Given that mainstream LLM training iterations typically span only a few seconds [22–26], intra-iteration topology reconfiguration is impractical. Under this constraint, maintaining a static topology throughout an iteration is a pragmatic strategy for current deployments [15–18]. Consequently, a priori engineering of a logical topology (i.e., the number of optical circuits allocated between Pod pairs [13, 27, 28]) tailored to absorb time-varying LLM traffic is critical for mitigating OCS-induced communication bottlenecks.

While such a priori engineering is imperative, tailoring a rigid logical topology to accommodate the dynamic traffic patterns extends far beyond simple volume-based allocation derived from the conventional traffic-matrix representation. Simply encoding traffic features into an aggregated traffic matrix within an iteration obscures the bursty concurrent communication demands dictated by parallelization strategies, thereby failing to account for the independent channels required for concurrent communication. To capture these transient peaks, existing approaches often employ fine-grained temporal snapshots of traffic. Yet, they typically revert to volume-based allocation within each time slice, aiming to drive dynamic reconfigurations (e.g., MixNet [19] and other practices in cloud data centers [13, 21, 29–31])—a path precluded by the aforementioned reconfiguration overhead. Ultimately, solving such an engineering problem hinges on strategically encoding the temporal dynamics of LLM traffic into the optimization formulation of the logical topology.

To address this engineering problem and construct an optimal logical topology, we propose DELTA, a DAG-aware, efficient framework for OCS logical topology optimization for AIDCs. We first analyze the spatiotemporal characteristics of LLM training traffic to identify the specific opportunities and optimization challenges in mapping these dynamics to topology construction (Section II). To address these challenges, we introduce a computation-communication DAG of

N. Ye, J. Liu, W. Sun, and W. Hu are with the State Key Laboratory of Photonics and Communications, Shanghai Jiao Tong University, Shanghai, China.

Corresponding author: Weiqiang Sun (E-mail: sunwq@sjtu.edu.cn).

LLM training that dynamically encodes the time-varying traffic patterns into the optimization formulation. This encoding allows the framework to exploit the full spectrum of traffic features while ensuring the resulting topology targets the exact bottlenecks governing the training iteration time. Based on this DAG, we formulate DELTA-Joint, an MILP model that jointly optimizes the topology and communication scheduling. Specifically, by pioneering a variable-length time interval formulation, DELTA-Joint averts the dimensionality curse inherent in conventional fixed-time-step methods. Moreover, by exploiting the temporal slack of non-critical communication tasks, the model incorporates a lexicographic objective to eliminate redundant port allocations without compromising the optimal iteration time (Section III). To scale to large-scale clusters, we design a dual-track acceleration strategy (Section IV). Specifically, we employ a search space pruning technique that reduces the problem complexity from quadratic to linear, compressing the MILP solving time to minutes. In parallel, we develop DELTA-Fast—a fast heuristic that yields high-quality topologies and provides a hot-start for the MILP, further accelerating MILP solving.

Evaluations on large-scale training workloads (e.g., the 671B-parameter DeepSeek model) show that DELTA reduces communication time by up to 17.5% compared to state-of-the-art traffic-matrix-based baselines. Furthermore, DELTA reduces optical port consumption by at least 20% without penalizing iteration time. By reallocating these freed ports to bottlenecked workloads, DELTA reduces their performance gap relative to ideal non-blocking electrical networks by up to 26.1%, enabling most workloads under optical switching to achieve nearly the performance of ideal electrical networks.

In summary, the key contributions of this work are threefold:

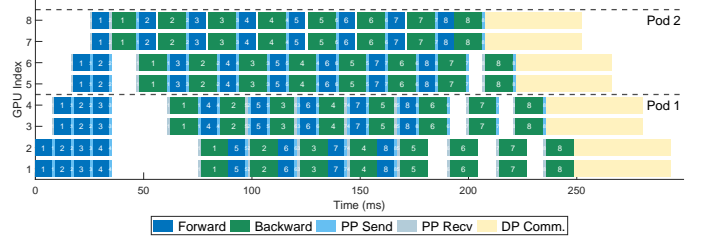
- We dynamically encode the time-varying traffic patterns of LLM training into the logical topology optimization formulation via a computation-communication DAG. This moves beyond traffic matrices, ensuring we fully exploit traffic characteristics while precisely targeting the bottlenecks that dictate iteration makespan.
- We significantly reduce the MILP solution space of DELTA by pioneering a variable-length time interval formulation. Combined with search space pruning (reducing complexity from quadratic to linear) and heuristic hot-starting, we solve the MILP within minutes, even at a thousand-GPU scale.
- We integrate a resource-saving paradigm into DELTA that exploits temporal slack in non-critical communication tasks to reduce optical port consumption without penalizing iteration time. Dynamically reallocating these freed ports enables most workloads under OCS to achieve performance nearly identical to ideal electrical networks.

II. BACKGROUND AND MOTIVATION

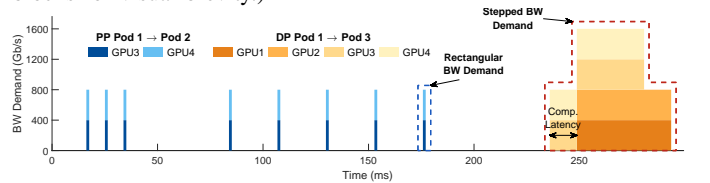
To motivate the design of DELTA, this section first characterizes the spatiotemporal traffic features of LLM training to identify topology optimization opportunities. We then articulate the algorithmic challenges in mapping these features to OCS configuration, followed by a review of related literature.

A. Features of LLM Training Traffic and Opportunities in Optimizing Logical Topology for OCS-AIDC

In contrast to the stochastic traffic patterns typical of cloud data centers, the communication within LLM training exhibits unique spatiotemporal characteristics driven by parallel strategies, namely Tensor (TP), Pipeline (PP), Data (DP), and Expert (EP) parallelism. Fig. 1 profiles a GPT-7B training iteration, revealing three key traffic features and corresponding optimization opportunities for OCS logical topologies:



(a) Execution trace of 1F1B scheduling on the first DP replica under a TP=2/PP=4/DP=2 parallelism configuration with 8 micro-batches per GPU (TP communications are subsumed into the forward/backward blocks for visual brevity.)



(b) Inter-pod bandwidth demand of Pod 1. Note the distinct profiles of PP (rectangular) and DP (stepped) bandwidth demand.

Fig. 1: Spatiotemporal profiling of GPT-7B training schedule and traffic under ideal 400 Gb/s network (GPUs are deployed uniformly across 4 Pods).

F1: Communication in LLM training features deterministic traffic demands governed by a computation-communication DAG. The model architecture and parallelization strategy jointly dictate the communication behavior during training, determining both the physical properties of the traffic and their causal dependencies. Consequently, the exact characteristics of communication tasks—including source-destination pairs, traffic volumes, and their temporal order—can be calculated before execution. As illustrated by the 1F1B execution trace in Fig. 1a, the launch time and scheduling order of each task are fully determined as a function of the 1F1B schedule.

Opportunity 1. *This predictability in LLM traffic enables proactive topology engineering, allowing the pre-allocation of network resources to match the bandwidth demands of each communication task.*

F2: LLM training generates bursty traffic, whose peak demand is driven by the scale of parallelism-induced concurrent flows. In contrast to the smooth traffic patterns typical of traditional cloud computing, LLM training traffic is characterized by burstiness and concurrency in the temporal dimension. As illustrated in Fig. 1b, inter-pod communication bandwidth demand surges during specific training process phases. Specifically, the concurrent transmission of activations

and gradients between model layers (PP communication) from GPU 3 and GPU 4 demands an aggregated inter-pod bandwidth of 2×400 Gb/s. And parameter synchronization between replicas (DP communication) involves successive communication from GPU 3&4 and GPU 1&2, resulting in a maximum bandwidth demand of 4×400 Gb/s.

Opportunity 2. *This burst concurrency implies that to alleviate congestion, resource allocation should prioritize provisioning independent physical channels (i.e., OCS lightpaths) that match flow concurrency, rather than simply allocating resources based solely on the aggregated traffic matrices.*

F3: DP communication exhibits time-varying concurrency and stepped bandwidth demand profiles. As illustrated in Fig. 1a, in hybrid parallel training, the backward pass propagates in reverse pipeline order, triggering gradient synchronization sequentially from the final stage back to the first. Consequently, the aggregated bandwidth demand manifests as a stepped envelope (Fig. 1b)—peaking exclusively during periods of flow overlap—rather than as a uniform rectangular burst typical of PP traffic. This intrinsic temporal staggering facilitates link time-multiplexing. Specifically:

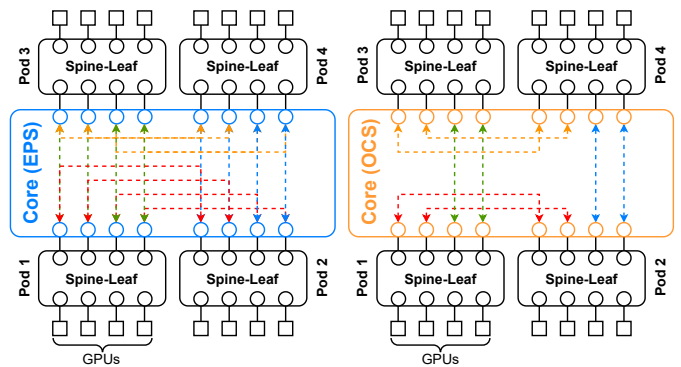
Opportunity 3. *Sufficiently staggering DP flows across pipeline stages shrinks peak-concurrency intervals, allowing us to provision fewer independent optical channels without exacerbating congestion.*

Opportunity 4. *Furthermore, the temporal slack of earlier DP flows enables dynamic bandwidth reallocation among overlapping DP tasks. Leveraging this slack helps accommodate bandwidth-intensive workloads under stricter capacity constraints without prolonging the global iteration makespan.*

B. Challenges of Optimizing Logical Topology for OCS-AIDC

The transition from the any-to-any connectivity of EPS (Fig. 2a) to the rigid point-to-point nature of OCS creates bottlenecks when destination-divergent flows (e.g., orthogonal PP and DP traffic) compete for limited optical exit ports (Fig. 2b). Under such hardware constraints, topology construction is essentially a constrained resource allocation problem. While utilizing the aforementioned opportunities for this problem is promising, capturing these benefits is non-trivial due to two distinct challenges in encoding the dynamic LLM training traffic patterns into the optimization formulation.

C1: Challenge in encoding shifting communication bottlenecks into the optimization for training iteration time reduction. In contrast to cloud data center workloads, where network throughput linearly correlates with application performance, the iteration time of LLM training is strictly determined by the most time-consuming sequence of causally chained computation and communication tasks (hereafter referred to as the critical path). Consequently, accelerating a specific communication flow yields no marginal gain if it resides outside this path. Compounding this issue, these bottlenecks are decision-dependent; optimizing one communication task can shift the critical path to a different sequence of tasks. Thus, a key challenge lies in mathematically encoding these shifting



(a) Any-to-any inter-pod paths established by the EPS. (b) Point-to-point inter-pod paths established by the OCS.

Fig. 2: Comparison of inter-pod connection patterns established by OCS and EPS for the multi-pod LLM training setup in Fig. 1.

bottlenecks into the topology optimization formulation, and ensuring the solver targets actual iteration-time reduction rather than merely maximizing aggregate network bandwidth.

C2: Challenge in encoding diverse and decision-dependent communication demands into topology optimization. Encoding the time-varying bandwidth requirements of LLM workloads (F2 and F3) into the optimization formulation presents two algorithmic hurdles. First, communication demands driven by different parallelization strategies exhibit distinct temporal behaviors, such as the stepped bandwidth demand envelopes of DP traffic versus the uniform, rectangular demand of PP traffic. Constructing a topology solely based on a traffic matrix fails to capture these temporal dynamics, thereby missing the temporal multiplexing opportunities created by the pipeline-induced staggering of DP flows (i.e., failing to exploit O3 and O4). Second, a circular dependency exists between topology decisions and traffic profiles. Specifically, any adjustment to the logical topology inherently alters transmission rates, which in turn stretches or compresses the actual flow durations. This non-linear coupling invalidates static optimization approaches, requiring a solver capable of dynamically tracking how topological decisions reshape the temporal demand landscape.

C. Related Work

OCS in cloud data centers. Existing studies have proposed various topology construction methods for the deployment of OCS in cloud data centers [13, 21, 28–35]. For instance, [13, 21, 29–31] construct logical topologies by exploiting long-term traffic pattern prediction to optimize network throughput or link utilization. Meanwhile, works such as [28, 32–35] focus on developing algorithms with polynomial time complexity to compute logical topology mapping and reconfiguration schemes that satisfy the physical port mapping constraints of OCS and maximize network throughput. However, these approaches target traditional cloud computing environments featuring stochastic, slow-varying traffic, prioritizing general network performance metrics over job-level execution times. Consequently, they are ill-suited for the deterministic,

bursty traffic of LLM training, where minimizing the iteration makespan is the primary objective.

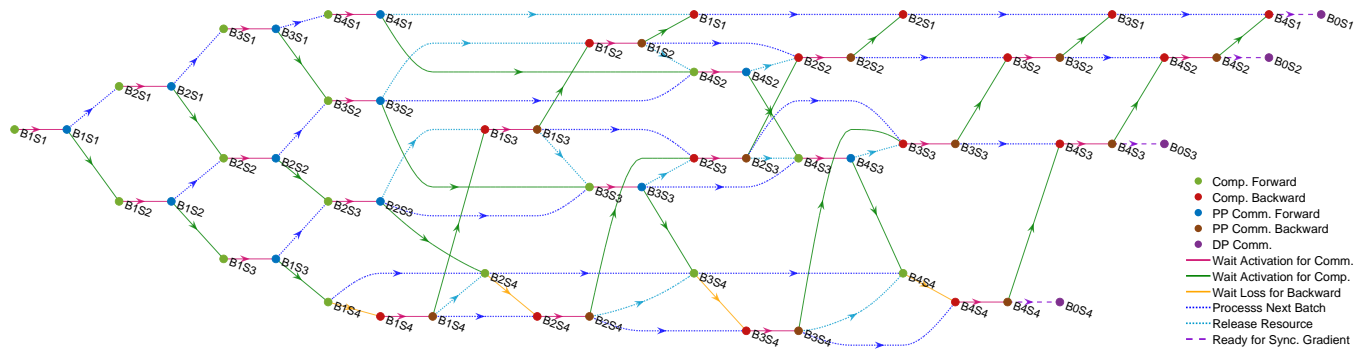
Introducing OCS into AI data centers. Recent studies have begun integrating OCS into AI data centers to optimize AI workload training time while reducing network costs [16, 19, 36–43]. Early works [36, 37] optimized OCS reconfiguration and multiplexed the optical circuit by exploiting the interleaved compute-communicate phases of distributed training, but focused exclusively on DP parameter synchronization. To further accelerate this synchronization process, [38–40] jointly optimize the schedule of optical circuit and in-network computing resources. However, such DP-centric and hardware-dependent designs lack the generality required for modern LLM training. Other studies [19, 41, 42] explore architectures where GPUs are directly connected to OCS, reconfiguring the topology based on traffic pattern predictions to optimize the All-to-All or All-Reduce communications required for EP or TP/DP. Yet, this approach is incompatible with the prevailing architectural paradigm of scaling clusters by interconnecting multiple pods via OCS. While the methods proposed in [16, 43] support OCS-based pod-level interconnection and are not restricted to specific workloads, their decision-making processes still rely on aggregated traffic matrices and fail to incorporate the iteration time of LLM training as an optimization objective. Consequently, they do not resolve the previously mentioned challenges **C1** and **C2**, which may lead to sub-optimal topological decisions—a critical limitation that our work specifically aims to overcome.

Computation-communication DAG-aware communication optimization. Existing works [44–49] emphasize the importance of leveraging computation-communication dependencies to optimize communication in LLM training. Specifi-

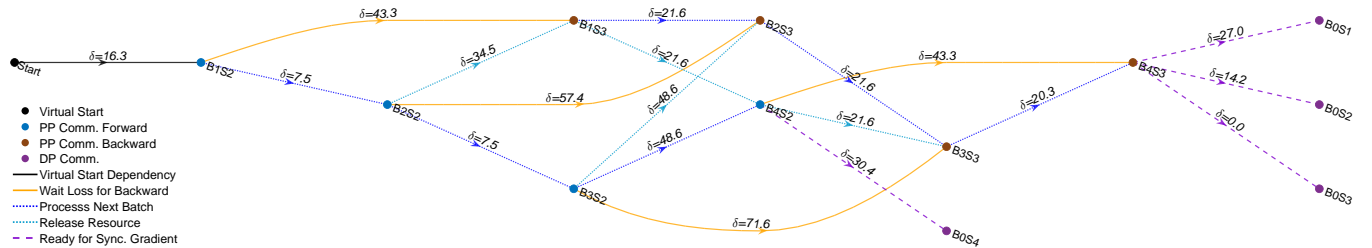
cally, studies such as [44–47] focus on the parameter synchronization phase in DP, utilizing priority-based scheduling for communication operations according to their dependency order to minimize synchronization stalls. For PP+DP hybrid parallelism, [48] groups and reorders the backward computation and corresponding gradient synchronization across different model layers; this removes a portion of DP communication from the critical path of the conventional 1F1B scheduling, enabling it to overlap with the computations of other layers. Furthermore, TriRace [49], an asynchronous pipeline scheduling approach, reschedules the communication required for PP and DP by analyzing the critical path within the DAG, thereby reducing the bubble rate in PP. While the aforementioned works primarily exploit DAG dependencies to schedule communication over a fixed network topology, our approach integrates DAG dependencies into logical topology optimization, tailoring the topology configuration to accelerate the LLM training.

III. COMPUTATION-COMMUNICATION DAG-AWARE OPTIMIZATION OF LOGICAL TOPOLOGY FOR OCS-AIDC

This section details our approach to optimizing the logical topology for OCS-AIDCs. To resolve the aforementioned challenges, our core strategy is to dynamically encode the time-varying, decision-dependent traffic patterns of LLM training into the optimization space via a computation-communication DAG. Building upon this DAG, we formulate an MILP model structured around variable-length time intervals to efficiently solve this logical topology optimization problem.



(a) Complete computation-communication DAG of an LLM training iteration.



(b) Reduced inter-pod communication DAG with intra-pod tasks merged into directed edges representing rigid intervals δ (ms).

Fig. 3: Complete computation-communication DAG and reduced inter-pod communication DAG of an LLM training iteration (setup identical to Fig. 1, but with 4 micro-batches). Node label “Bbs” indicates the processing of micro-batch b at stage s .

A. Encoding LLM Training Traffic Dynamics via the Computation-Communication DAG

Fig. 3a illustrates the DAG corresponding to the LLM training iteration shown in Fig. 1a. For clarity, the micro-batch size is reset to 4, and each pair of synchronously executed PP send and receive tasks is consolidated into a single node. In this DAG, each computation or communication task is represented as a node with a specific execution duration, and the directed edges enforce strict causal dependencies between tasks. Specifically, these dependencies fall into three categories: (1) data dependencies dictated by the computational graph of the LLM itself (*Wait Activation/Loss for Comm./Comp./Backward*); (2) scheduling dependencies governed by the micro-batch scheduling mechanism in PP (*GPU Process Next Batch* and *Release GPU Resource*); and (3) gradient dependencies induced by waiting for the backward pass of the final micro-batch to complete before gradient synchronization (*Ready for Sync. Gradient*). Crucially, once the model architecture and parallelization strategy are defined, this topology-agnostic DAG is determined.

The cornerstone of our approach is encoding the time-varying traffic patterns via this computation-communication DAG. Specifically, we formulate the execution of a training iteration as a precedence-constrained scheduling problem to minimize the overall iteration makespan C . This makespan is strictly defined by the length of the critical path:

$$C = \sum_{m \in \mathcal{E}_{\text{crit}}} \tau_m, \quad (1)$$

where $\mathcal{E}_{\text{crit}}$ denotes the critical path of the DAG, and τ_m represents the duration of individual tasks. Within this formulation, we treat the start and completion times of each task as decision variables bounded by the DAG’s edges. The topology decisions dictate the bandwidth, which in turn determines the duration of individual tasks (τ_m). Constrained by the causal dependencies defined by the DAG, any change in a task’s duration cascades to its successors, thereby shifting the overall temporal distribution of traffic. By natively encoding this topology-traffic coupling into the decision space via this DAG, our formulation intrinsically captures the decision-dependent communication demands (addressing **C2**), while simultaneously ensuring that minimizing the objective directly targets the exact communication bottlenecks governing the iteration makespan (addressing **C1**).

Notably, in the logical topology optimization problem for OCS-AIDC, the design decisions affect only the durations of inter-pod communication tasks. Therefore, explicitly modeling intra-pod computation or communication tasks—whose execution times are independent of the inter-pod topology—is redundant. To reduce complexity, we perform graph reduction on Fig. 3a, yielding the reduced DAG shown in Fig. 3b. Specifically, for any two inter-pod communication tasks m_{pre} and m that are separated solely by intra-pod tasks in the original DAG, the intermediate intra-pod tasks are equivalently replaced by a weighted directed edge (we introduce a virtual inter-pod communication task occurring at $t = 0$ to handle the intra-pod tasks preceding the first inter-pod communication task in the same manner). The weight of this edge, denoted

by $\delta_{m_{\text{pre}} \rightarrow m}$, equals the sum of the execution times of these intra-pod tasks. Accordingly, C can be reformulated as:

$$C = \sum_{m \in \mathcal{E}_{\text{crit}}^{\text{inter-pod}}} \tau_m + \sum_{m_{\text{pre}}, m \in \mathcal{E}_{\text{crit}}^{\text{inter-pod}}} \delta_{m_{\text{pre}} \rightarrow m}, \quad (2)$$

where $\mathcal{E}_{\text{crit}}^{\text{inter-pod}}$ denotes the inter-pod tasks on $\mathcal{E}_{\text{crit}}$. Eq. (2) provides a reduced-complexity model for LLM training iteration time, which will be incorporated into the mathematical formulation of the topology optimization problem in the subsequent section.

B. MILP Formulation with Variable-Length Time Interval for Logical Topology Optimization

Conventional network optimization literature [39, 50–55] typically relies on fixed-time-step formulations to capture the bandwidth reallocation and rate variations induced by the dynamic arrival and completion of communication tasks. However, this approach imposes a trade-off between temporal precision and computational efficiency: coarse-grained discretization obscures transient traffic variations, whereas fine-grained discretization inflates the decision space, rendering the model computationally intractable. Empirically, solving the fixed-time-step MILP (detailed in Appendix A) for small-scale workloads—where training iterations span only hundreds of milliseconds—still requires tens of hours at a 0.1-ms resolution, precluding its real-world application.

To overcome this computational bottleneck, we pioneer a variable-length time interval modeling approach inspired by the methodology of Discrete Event Simulation (DES), as illustrated in Fig. 4. In a DES paradigm, the system state—specifically, the task activation state ($y_{m,k}$) and flow rates (the ratio of data volume $w_{m,k}$ to interval duration Δ_k)—remains entirely static between state-transition events, which in our context correspond to the initiation (S_m) and completion (C_m) of communication tasks. Therefore, instead of uniformly slicing the time horizon, we can derive the temporal discretization points (t_k) solely from the occurrences of these events, dynamically partitioning the timeline into a sequence of K variable-length intervals.¹

Leveraging the stability within each of these K intervals allows a concise set of variables (e.g., $y_{m,k}$, $w_{m,k}$, and Δ_k) to sufficiently characterize the entire temporal horizon, obviating the need to track the system at fixed, fine-grained time steps. This approach fundamentally decouples the problem size from temporal granularity, thereby avoiding the variable explosion inherent in high-resolution time slicing and significantly reducing the MILP solution space. The rigorous mathematical formulation is detailed below.

Input Parameters:

- \mathcal{P} : The set of all Pods in the OCS-AIDC.

¹Theoretically, because each task contributes exactly two state-transition timestamps (initiation and completion), setting $K \leq 2|\mathcal{M}| - 1$ (where \mathcal{M} is the set of all tasks) guarantees capturing all state transitions. In practice, K is profiled from a baseline simulation and is typically much smaller, as synchronized tasks (e.g., equivalent communication tasks executing concurrently within separate DP replicas in identical network environments) share identical event timestamps.

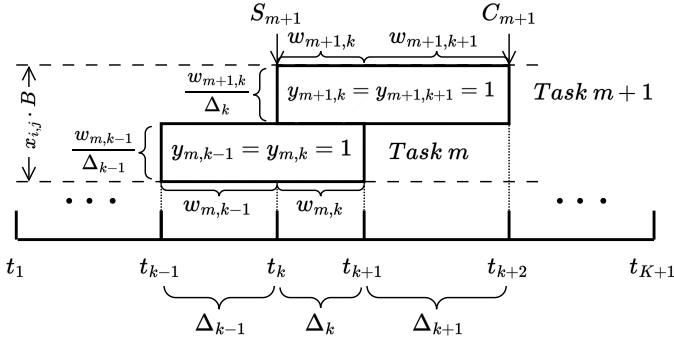


Fig. 4: Primary decision variables and their relationships within the variable-length time interval MILP formulation.

- \mathcal{G} : The set of all GPUs in the OCS-AIDC.
- \mathcal{M} : The set of inter-pod communication tasks involved in a single training iteration. An element $m \in \mathcal{M}$ is defined by a 6-tuple $m \triangleq (i_m, j_m, F_m, V_m, \mathcal{G}_m^{\text{src}}, \mathcal{G}_m^{\text{dst}})$, representing the source Pod, destination Pod, number of concurrent flows (where communication between a pair of GPUs corresponds to one flow), data volume, source GPU set, and destination GPU set, respectively. Notably, to reduce the problem scale, synchronous communication tasks triggered from multiple GPUs and sharing the identical source-destination Pod pair (e.g., PP/DP communication tasks from all GPUs within the same stage) are aggregated into a single communication task, with its flow count accumulated accordingly. Note that **O2** is exploited through the joint incorporation of F_m and V_m into the formulation, ensuring that resource allocation matches instantaneous flow concurrency rather than relying solely on data volume.
- \mathcal{D} : The set of temporal dependencies among communication tasks. The element $(m_{\text{pre}}, m, \delta_{m_{\text{pre}} \rightarrow m}) \in \mathcal{D}$ indicates that the successor task m can only start after a rigid time interval of $\delta_{m_{\text{pre}} \rightarrow m}$ following the completion of the predecessor task m_{pre} . Note that incorporating the a priori knowledge of \mathcal{M} and \mathcal{D} exploits **O1** for proactive topology engineering and **O3** for DP flow-staggering-aware topology optimization.
- $\Phi_{\text{src}}(g), \Phi_{\text{dst}}(g)$: The set of communication tasks originating from and destined for GPU g .
- U_p : The maximum number of available OCS ports for the training job in Pod p , generally constrained to the number of allocated GPUs in that Pod for fairness purposes.
- $L_{i,j}$: The number of binary bits required to represent the maximum number of optical circuits between Pod i and Pod j , defined as $\lfloor \log_2(\min(U_i, U_j)) \rfloor + 1$.
- B : The maximum network injection bandwidth of a single NIC, which is assumed to be identical to the bandwidth capacity of a single OCS port.
- K : The maximum index of time intervals within the considered time horizon.
- M : A large positive constant.

Unless otherwise specified, all indices i, j range over the set of \mathcal{P} , g ranges over the set of \mathcal{G} , k ranges over the set of $\{1, \dots, K\}$, and m belongs to the set of \mathcal{M} .

Decision Variables:

- $x_{i,j}$: An integer variable denoting the number of optical circuits/ports allocated between Pod i and Pod j .
- $\beta_{i,j,b}$: A binary auxiliary variable that equals 1 if the b -th bit in the binary representation of $x_{i,j}$ is 1, and 0 otherwise.
- t_k : A continuous variable denoting the start time of the k -th time interval.
- Δ_k : A continuous variable denoting the duration of the k -th time interval.
- $\rho_{i,j,b,k}$: A continuous auxiliary variable. If $\beta_{i,j,b} = 1$, this variable equals to Δ_k ; otherwise, it evaluates to 0.
- $w_{m,k}$: A continuous variable indicating the data volume transmitted by task m during time interval k . Note that by formulating both $w_{m,k}$ and Δ_k as decision variables, the following MILP inherently exploits **O4** to optimize the transmission rates of competing flows.
- $y_{m,k}$: A binary variable indicating whether task m is active during time interval k .
- $s_{\text{flag}_{m,k}}$: A binary auxiliary variable indicating whether task m is initiated at time interval k .
- S_m, C_m : Continuous variables denoting the start time and completion time of task m , respectively.
- C : A continuous variable denoting the iteration time of LLM training.
- $u_{i,j,k}$: A continuous auxiliary variable denoting the reference per-flow data transmission volume across the aggregated optical circuits between Pod i and Pod j during the k -th time interval. It facilitates the fair distribution (optional) of bandwidth across all active tasks sharing this inter-pod connection.

Objective:

The primary optimization objective is to minimize the iteration time of the training task:

$$\min C. \quad (3)$$

To conserve optical port resources by eliminating redundant allocations on non-critical paths (exploiting **O4**), an optional lexicographic objective is introduced to minimize the total allocated ports. Letting C^* denote the optimal makespan obtained in Eq. (3), this secondary objective is defined as:

$$\min \sum_{i \in \mathcal{P}} \sum_{j \in \mathcal{P}, j \neq i} x_{i,j}, \quad \text{s.t. } C \leq C^*. \quad (4)$$

Constraints:

1) Topology-Related Constraints:

$$\begin{cases} \sum_{j \in \mathcal{P}, j \neq i} x_{i,j} \leq U_i, & \forall i. \\ \sum_{i \in \mathcal{P}, i \neq j} x_{i,j} \leq U_j, & \forall j. \end{cases} \quad (5)$$

Eq. (5) ensures that the total number of outgoing and incoming logical connections for any Pod is constrained by its available transmission ports U_i and receiving ports U_j , respectively.

$$x_{i,j} = x_{j,i}, \quad \forall i, j. \quad (6)$$

Eq. (6) ensures that every directed logical link is accompanied by a reciprocal circuit, satisfying the bidirectional connectivity required for practical network operation [28].

$$x_{i,j} = \sum_{b=0}^{L_{i,j}-1} 2^b \cdot \beta_{i,j,b}, \quad \forall i, j. \quad (7)$$

Eq. (7) expands $x_{i,j}$ into its binary representation to facilitate the subsequent linearization of the bilinear term $x_{i,j} \cdot \Delta_k$. Specifically, we adopt binary rather than unary expansion to reduce the dimensionality of b from U_p down to $\log_2 U_p$.

2) *Optical Circuit and NIC Capacity-Related Constraints:*

$$\begin{cases} \rho_{i,j,b,k} \leq M \cdot \beta_{i,j,b}, \\ \rho_{i,j,b,k} \leq \Delta_k, \\ \rho_{i,j,b,k} \geq \Delta_k - M \cdot (1 - \beta_{i,j,b}), \end{cases} \quad \forall i, j, \forall k, \forall b \in \{0, \dots, L_{i,j} - 1\}. \quad (8)$$

Eq. (8) employs the Big-M method [56] to linearize the bilinear term $\beta_{i,j,b} \cdot \Delta_k$. Specifically, the formulation constrains $\rho_{i,j,b,k}$ to equal Δ_k when $\beta_{i,j,b} = 1$, and enforces $\rho_{i,j,b,k} = 0$ when $\beta_{i,j,b} = 0$, thereby ensuring the equivalence $\rho_{i,j,b,k} = \beta_{i,j,b} \cdot \Delta_k$.

$$\sum_{m \in \mathcal{M}(i,j)} w_{m,k} \leq B \cdot \sum_{b=0}^{L_{i,j}-1} (2^b \cdot \rho_{i,j,b,k}), \quad \forall k, \forall i, j. \quad (9)$$

Eq. (9) bounds the aggregated traffic rate in Δ_k by the total bandwidth of the allocated optical circuits from Pod i to Pod j . Here, $\mathcal{M}(i,j)$ denotes the set of tasks originating from Pod i and destined for Pod j . Note that the term $\sum_{b=0}^{L_{i,j}-1} (2^b \cdot \rho_{i,j,b,k})$ is introduced to represent the binary expansion and linearization of the bilinear term $x_{i,j} \cdot \Delta_k$.

$$\begin{cases} \sum_{m \in \Phi_{\text{src}}(g)} \frac{w_{m,k}}{F_m} \leq B \cdot \Delta_k, & \forall k, \forall g. \\ \sum_{m \in \Phi_{\text{dst}}(g)} \frac{w_{m,k}}{F_m} \leq B \cdot \Delta_k, & \forall k, \forall g. \end{cases} \quad (10)$$

Eq. (10) ensures that the aggregated injection and reception data volume of each GPU during interval k must not exceed the maximum data theoretically transferable by the NIC bandwidth B . This constraint assumes a one-to-one mapping between GPUs and NICs, regulating both the outgoing tasks in $\Phi_{\text{src}}(g)$ and the incoming tasks in $\Phi_{\text{dst}}(g)$.

3) *Data Conservation and Task Activation Constraints:*

$$\sum_{k=1}^K w_{m,k} = V_m, \quad \forall m. \quad (11)$$

Eq. (11) guarantees that the sum of the data transmitted by a task m across all time intervals exactly equals its predefined total data volume, V_m .

$$w_{m,k} \leq V_m \cdot y_{m,k}, \quad \forall m, k. \quad (12)$$

Eq. (12) restricts a task to transmit data strictly during the time intervals in which it is active (i.e., $y_{m,k} = 1$). If a task is inactive ($y_{m,k} = 0$), its transmission volume $w_{m,k}$ is forcefully constrained to 0.

$$\begin{cases} s_flag_{m,k} \geq y_{m,k} - y_{m,k-1}, & \forall m, k \quad (\text{setting } y_{m,0} = 0). \\ \sum_{k=1}^K s_flag_{m,k} = 1, & \forall m. \end{cases} \quad (13)$$

Eq. (13) introduces $s_flag_{m,k}$ to identify the activation event (rising edge) of task m . By limiting the total number of such events to one, the constraint prevents task suspension, ensuring that each task occupies a single, contiguous time block.

4) *Temporal Boundary and Mapping Constraints:*

$$\Delta_k = t_{k+1} - t_k, \quad \forall k. \quad (14)$$

Eq. (14) defines the duration of the k -th time interval, Δ_k , as the difference between adjacent temporal points.

$$\begin{cases} S_m \leq t_k + M \cdot (1 - y_{m,k}), & \forall m, k. \\ C_m \geq t_{k+1} - M \cdot (1 - y_{m,k}), & \forall m, k. \end{cases} \quad (15)$$

Eq. (15) defines the temporal boundaries of task m based on its active intervals. By utilizing the Big-M method, it ensures that the interval $[S_m, C_m]$ encompasses all time slots Δ_k where the task is scheduled to transmit ($y_{m,k} = 1$).

5) *Inter-Pod Communication DAG Constraints:*

$$S_m \geq C_{m_{\text{pre}}} + \delta_{m_{\text{pre}} \rightarrow m}, \quad \forall (m_{\text{pre}}, m, \delta_{m_{\text{pre}} \rightarrow m}) \in \mathcal{D}. \quad (16)$$

Eq. (16) guarantees that the execution order strictly adheres to the reduced inter-pod communication DAG. Specifically, it ensures that any subsequent task m is initiated only after the completion of its predecessor m_{pre} and the subsequent elapse of the time interval $\delta_{m_{\text{pre}} \rightarrow m}$.

6) *Flow Fairness Constraints (Optional for Comparison):*

$$\begin{cases} \frac{w_{m,k}}{F_m} - u_{i,j,k} \leq M \cdot (1 - y_{m,k}), \\ u_{i,j,k} - \frac{w_{m,k}}{F_m} \leq M \cdot (1 - y_{m,k}), \end{cases} \quad \forall i, j, \forall m \in \mathcal{M}(i,j), \forall k. \quad (17)$$

Eq. (17) is an optional constraint that simulates conventional fair-sharing mechanisms by compelling concurrently active tasks ($y_{m,k} = 1$) traversing the same inter-pod connection to transmit an equal volume of data per flow ($u_{i,j,k}$). It is introduced as a comparative baseline to quantify the performance gains of the optimized rate control strategy against the conventional fair-sharing policy.

7) *Objective Function Constraint:*

$$C \geq C_m, \quad \forall m. \quad (18)$$

Eq. (18) defines the LLM training iteration time C as the upper bound of all individual task completion times C_m . Note that, rather than explicitly modeling C using the critical-path-based formulation in Eq. (2), Eq. (18) relies on the linear temporal constraints derived from the DAG \mathcal{D} (Eq. (16)) to express C in an MILP-tractable format.

IV. ACCELERATION OF MILP SOLVING AND DESIGN OF HEURISTIC ALGORITHMS

Despite the substantial simplification achieved through the reduced inter-pod communication DAG and variable-length time interval modeling, directly solving the proposed MILP remains computationally intractable for LLM training workloads spanning multiple Pods and thousands of GPUs. To overcome this, this section introduces a dual-track acceleration approach. First, we incorporate domain-specific strategies to reduce the MILP scale. In parallel, we develop a fast heuristic search algorithm for efficient hot-starting. Collectively, these strategies guarantee rapid convergence to a high-quality solution within minutes, even at the thousand-GPU scale.

A. Strategies for Accelerating MILP Solving

The scale of the MILP is primarily governed by the task-time decision variables ($w_{m,k}$, $y_{m,k}$, and $s_flag_{m,k}$), which exhibit a quadratic growth of $\mathcal{O}(|\mathcal{M}|^2)$ since the interval count K scales linearly with the task count $|\mathcal{M}|$. In contrast, the scale of the topology and capacity variables ($x_{i,j}$, $\beta_{i,j,b}$, $\rho_{i,j,b,k}$, and $u_{i,j,k}$) is constrained. While the number of possible pairs (i, j) is theoretically bounded by the square of the Pod count ($|\mathcal{P}|^2$), the sparsity of LLM communication pairs substantially reduces the actual number of instantiated spatial variables. Coupled with the logarithmic bound of the binary expansion index b , the total number of these variables scales at most linearly with the interval count K (i.e., $\mathcal{O}(|\mathcal{M}|)$). Consequently, they constitute a negligible fraction of the model size. Therefore, our acceleration strategies specifically target the $\mathcal{O}(|\mathcal{M}|^2)$ variable explosion induced by the task-time variables.

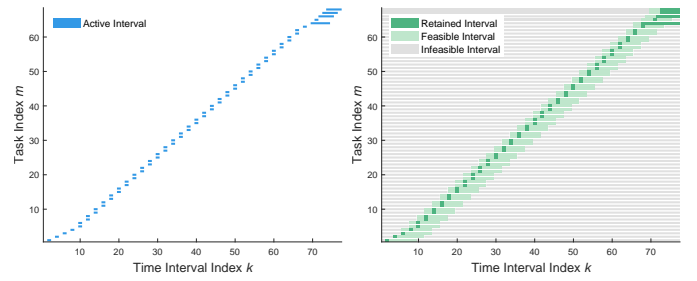
1) Reducing Total Task Count by Isomorphism and Independence of DP Replicas:

We first project the multi-replica optimization problem onto a single-replica domain by leveraging the isomorphism and independence of DP replicas to mitigate the $\mathcal{O}(|\mathcal{M}|^2)$ complexity associated with task-time variables. Specifically, when different DP replicas are deployed in identical network environments, their communication tasks are theoretically synchronized. By formulating the MILP for a single reference replica and mapping the resulting topology configurations and schedules across the others, the global task count $|\mathcal{M}|$ can be reduced to the scale of a single replica. Conversely, when DP replicas span heterogeneous networks, we exploit the decoupled nature of their execution. Aside from parameter synchronization tasks, the operations within each replica are independent of the others. This allows the global optimization to be decomposed into parallel single-replica sub-problems. To satisfy the DP synchronization barrier, the schedule of the bottleneck replica—which initiates the synchronization phase last—is established as the global temporal baseline to align the DP communication across all replicas. Ultimately, regardless of the deployment scenario, this methodology guarantees solution validity and global iteration time optimality while successfully reducing the dimensionality of task-time decision variables from a $\mathcal{O}(|\mathcal{M}|^2)$ complexity to a single-replica-related $\mathcal{O}(|\mathcal{M}_{\text{single-replica}}|^2)$ scale.

2) Reducing search space by Task-Time Domain Pruning:

To further reduce computational complexity, we prune the search space of task-time related decision variables (i.e., $w_{m,k}$, $y_{m,k}$, and $s_flag_{m,k}$). As illustrated by Fig. 5a, within the model and parallel configuration defined in Fig. 1a, each inter-pod communication task for each DP replica occupies only a small fraction of the total time intervals in practice.² Given these observations, it is reasonable to infer that the optimal solution of this MILP will exhibit a sparse structure for $y_{m,k}$ and its associated variables $w_{m,k}$, $s_flag_{m,k}$.

²It should be noted that because some inter-pod communication tasks overlap in time (as shown in Fig. 1a, e.g., the forward PP communications for micro-batches 4, 5, 6, 7, 8 on Stage 2 and Stage 3 completely overlap with the backward PP communications for micro-batches 2, 3, 4, 5, 6), the total number of time intervals K is less than $2|\mathcal{M}_{\text{single-replica}}| - 1$.



(a) Active intervals of tasks under a baseline network in practice. (b) Retained intervals refined by DAG and anchor-guided pruning.

Fig. 5: search space reduction for MILP via index pruning (LLM training setup as in Fig. 1, but with 32 micro-batches).

Specifically, the temporal dependencies defined by the set \mathcal{D} impose strict boundaries on the feasible active intervals for communication tasks. Dictated by these dependencies, a task cannot be activated too early, as this would inevitably force its predecessors into invalid time intervals (i.e., interval indices < 1). Conversely, given a total interval count K , a task cannot remain active too late without pushing its subsequent tasks into invalid time intervals (i.e., indices $> K$) (provided the assigned K accommodates the theoretical optimal solution, pruning these states preserves optimality). Leveraging this property, we apply a topological sorting algorithm to \mathcal{D} —computing the longest paths from the global source and sink nodes of the DAG to each task—to determine the earliest and latest allowable interval indices for every task. Consequently, the corresponding decision variables ($w_{m,k}$, $y_{m,k}$, and $s_flag_{m,k}$) can be strictly constrained to 0 outside this feasible temporal window, thereby substantially reducing the search space. The pruning effect of this strategy on the $m - k$ search space is illustrated by the light green regions in Fig. 5b.

While the preceding topological sorting establishes boundaries based on whole-graph-wide longest paths, relying solely on it yields overly conservative search spaces (detailed in Appendix B). From a local-task-centric perspective, as observed from Fig. 3b and Fig. 5a, the dependencies in \mathcal{D} strictly constrain the execution of intermediate tasks: a task m cannot overlap with the state transitions of its predecessors or successors. Driven by this strict causal ordering, an intermediate task typically monopolizes a complete time interval, leaving minimal room for shifts within the discrete interval sequence and rendering its active index range highly deterministic. Consequently, a lightweight baseline simulation (Fig. 5a) can approximate this range. Exploiting this predictability, we extract index bounds $[k_m^{\text{start}}, k_m^{\text{end}}]$ for each intermediate task m from the profiling results (to accommodate potential index encroachments among tasks sharing identical topological orders, we introduce a slight redundancy margin when calculating $[k_m^{\text{start}}, k_m^{\text{end}}]$). By integrating these anchoring bounds with longest-path-derived boundaries, we tightly confine the allowable active indices, further pruning the $m - k$ search space as illustrated by the dark green regions in Fig. 5b. The complete algorithm workflow is presented in Alg. 1. Since most tasks are intermediate tasks (Fig. 3b), bounding their indices significantly tightens the entire MILP

scale. Through a cascade effect, this tightening further prunes the indices of DP tasks. Ultimately, the combined restriction on both intermediate and DP tasks reduces the scale of task-time decision variables from $\mathcal{O}(|\mathcal{M}|^2)$ to $\mathcal{O}(|\mathcal{M}|)$.

Collectively, by synergistically applying the aforementioned task reduction and search space pruning strategies, we guarantee rapid convergence to a high-quality solution within minutes, even at the thousand-GPU scale.

Algorithm 1 TaskTimeIndexPruning

Input: \mathcal{M} , \mathcal{D} , K , anchors $\tilde{k}_m^{\text{start}}$ and \tilde{k}_m^{end} . Let $\mathcal{M}_{\text{succ}} \triangleq \{m \in \mathcal{M} \mid \exists(u, v, \delta) \in \mathcal{D}\}$ denote the subset of tasks that have successor tasks.

Output: Pruned upper bounds $UB(\cdot)$ for decision variables.

▷ **Step 1: Initialization & Anchoring**

- 1: **for each** $m \in \mathcal{M}$ **do** $k_m^{\min} \leftarrow 1$, $k_m^{\max} \leftarrow K$
- 2: **for each** $m \in \mathcal{M}_{\text{succ}}$ **do** $k_m^{\min} \leftarrow \tilde{k}_m^{\text{start}}$, $k_m^{\max} \leftarrow \tilde{k}_m^{\text{end}}$
- 3: Compute in-degree $deg_{\text{in}}(m)$ and out-degree $deg_{\text{out}}(m)$ based on \mathcal{D} .

▷ **Step 2: Forward Bounds Propagation (Earliest Start)**

- 4: $\mathcal{Q} \leftarrow \{m \in \mathcal{M} \mid deg_{\text{in}}(m) = 0\}$
- 5: **while** $\mathcal{Q} \neq \emptyset$ **do**
- 6: $u \leftarrow \mathcal{Q}.\text{pop}()$
- 7: **for each** $(u, v, \delta) \in \mathcal{D}$ **do**
- 8: $k_v^{\min} \leftarrow \max(k_v^{\min}, k_u^{\min} + (\delta > 0 ? 2 : 1))$
- 9: $deg_{\text{in}}(v) \leftarrow deg_{\text{in}}(v) - 1$; **if** $deg_{\text{in}}(v) == 0$ **then**
 $\mathcal{Q}.\text{push}(v)$
- 10: **end for**
- 11: **end while**

▷ **Step 3: Backward Bounds Propagation (Latest End)**

- 12: $\mathcal{Q} \leftarrow \{m \in \mathcal{M} \mid deg_{\text{out}}(m) = 0\}$
- 13: **while** $\mathcal{Q} \neq \emptyset$ **do**
- 14: $v \leftarrow \mathcal{Q}.\text{pop}()$
- 15: **for each** $(u, v, \delta) \in \mathcal{D}$ **do**
- 16: $k_u^{\max} \leftarrow \min(k_u^{\max}, k_v^{\max} - (\delta > 0 ? 2 : 1))$
- 17: $deg_{\text{out}}(u) \leftarrow deg_{\text{out}}(u) - 1$; **if** $deg_{\text{out}}(u) == 0$ **then**
 $\mathcal{Q}.\text{push}(u)$
- 18: **end for**
- 19: **end while**

▷ **Step 4: Variable Domain Pruning**

- 20: **for each** $m \in \mathcal{M}$ **do**
 - 21: $\mathcal{K}_{\text{invalid}} \leftarrow \{1, \dots, k_m^{\min} - 1\} \cup \{k_m^{\max} + 1, \dots, K\}$
 - 22: **for each** $k \in \mathcal{K}_{\text{invalid}}$ **do**
 $UB(y_{m,k}), UB(w_{m,k}), UB(s_{\text{flag}_{m,k}}) \leftarrow 0$
 - 23: **end for**
 - 24: **return** $UB(\cdot)$
-

B. Simulation-Based Heuristic Search Algorithm

Although the accelerated MILP in Section IV-A efficiently achieves joint topology and flow-rate optimization, broader scenarios—like GPU-resource allocation co-optimization in multi-tenant clusters—demand frequent invocations of the topology optimizer. To this end, we propose a fast, simulation-based heuristic search algorithm (DELTA-Fast). The key idea

is to decouple the search space by offloading the constraint-solving process of the cumbersome task-time dimensions (i.e., $y_{m,k}$, $w_{m,k}$, and Δ_k) to a lightweight DES engine, thereby avoiding computationally expensive joint searches across all variables. Specifically, an outer-loop genetic algorithm optimizes the logical topology ($x_{i,j}$), while an inner-loop DES chronologically simulates tasks based on DAG dependencies. Through a single simulation pass, it implicitly determines valid values for these temporal and task-state variables, naturally satisfying all constraints. Although this decoupling sacrifices the dynamic joint optimization of flow rates (degenerating to a fair-sharing mechanism), it effectively mitigates computational complexity, enabling the rapid generation of high-quality topology candidates for upper-level co-optimization frameworks. Furthermore, since the DES execution trace is isomorphic to the MILP’s event-driven formulation, the simulated results seamlessly map to an initial feasible solution, providing an efficient hot-start for the MILP. To further accelerate the search process, we design DELTA-Fast around two core components: a DAG-aware search space pruning strategy and a domain-adapted genetic algorithm.

1) *DAG-Aware search space Pruning:*

To prune the topology search space, we eliminate redundant capacity allocations by jointly exploiting physical and logical constraints. Physically, NIC-bound GPU data injection limits render any optical circuits (x_{ij}) exceeding the maximum concurrent inter-Pod flows redundant (exploiting **O2**). Logically, the DAG \mathcal{D} explicitly prohibits temporally dependent inter-Pod tasks from executing concurrently. Motivated by these observations, we propose Alg. 2 to estimate the maximum concurrent communication pairs per inter-pod connection to establish an upper bound for x_{ij} : First, similar to Alg. 1, we use \mathcal{D} and a coarse estimated iteration time upper bound \hat{T}_{up} to derive the earliest start time (EST_m) and latest completion time (LCT_m) for each task m (Line 2, detailed in Alg. 4 in Appendix C). Next, computing the transitive closure \mathcal{R} of \mathcal{D} identifies all dependency-linked, mutually exclusive task pairs (Line 3). Subsequently, for each inter-pod connection (u, v) , we merge and sort the temporal boundaries (EST and LCT) of all associated tasks into a discrete interval sequence T (Lines 5-6). Scanning each interval, the algorithm extracts active tasks \mathcal{A} to construct a conflict graph G , where tasks act as vertices, flow counts as vertex weights, and mutual exclusivity relations as edges (Lines 8-12). Since mutually exclusive tasks cannot run in parallel, the maximum concurrent flow per interval equals the Maximum Weight Independent Set (MWIS) of G . Finally, the peak MWIS across all intervals defines the tight capacity upper bound $\bar{X}_{u,v}$ (Lines 13-14), significantly compressing the topology search space.

2) *Simulation-Based Domain-Adapted Genetic Algorithm:*

To efficiently navigate the constrained topology search space and accelerate convergence, we develop a domain-adapted genetic algorithm that integrates a fast DES engine driven by the reduced DAG \mathcal{D} for rapid iteration time evaluation, alongside a topology repair mechanism utilizing the capacity upper bounds \bar{X} to restore the physical feasibility of invalid offspring. As illustrated in Alg. 3, after initializing a population of feasible topologies strictly bounded by physical port

Algorithm 2 XUpperBoundEstimation

Input: \mathcal{M} , \mathcal{D} , estimated iteration time upper bound \hat{T}_{up} .

Output: Upper bound matrix \bar{X} for x_{ij} .

▷ **Step 1: Initialization & Preprocessing**

- 1: Initialize \bar{X} as a zero matrix for all pod pairs
- 2: $[\text{EST}, \text{LCT}] \leftarrow \text{CalTaskTimeWindows}(\mathcal{M}, \mathcal{D}, \hat{T}_{up})$
- 3: $\mathcal{R} \leftarrow \text{TransitiveClosure}(\mathcal{D})$ ▷ via matrix squaring

▷ **Step 2: Capacity Bound Computation**

- 4: **for each** inter-pod connection (u, v) **do**
- 5: $\mathcal{M}_{u,v} \leftarrow \{m \in \mathcal{M} \mid \text{task } m \text{ traverses } (u, v)\}$
- 6: $T \leftarrow \text{Sort}(\text{Unique}(\{\text{EST}_m, \text{LCT}_m \mid m \in \mathcal{M}_{u,v}\}))$
- 7: **for** $k \leftarrow 1$ **to** $|T| - 1$ **do**
- 8: $t_{\text{mid}} \leftarrow (T[k] + T[k + 1]) / 2$
- 9: $\mathcal{A} \leftarrow \{m \in \mathcal{M}_{u,v} \mid \text{EST}_m \leq t_{\text{mid}} < \text{LCT}_m\}$
- 10: **if** $\mathcal{A} \neq \emptyset$ **then**
- 11: ▷ **Construct the conflict graph for MWIS**
- 12: $G \leftarrow \text{Graph}(\text{Vertices} = \mathcal{A}, \text{Weights} = F_{m \in \mathcal{A}}, \text{Edges} = \mathcal{R}|_{\mathcal{A}})$
- 13: $c_{\text{max}} \leftarrow \text{SolveMWIS}(G)$ ▷ Solve MWIS
- 14: $\bar{X}_{u,v} \leftarrow \max(\bar{X}_{u,v}, c_{\text{max}})$
- 15: **end if**
- 16: **end for**
- 17: **end for**
- 18: **return** \bar{X}

limits U and capacity bounds \bar{X} (Line 1, detailed in Alg. 5 in Appendix D), iteration time (fitness) is evaluated in parallel via the DAG-aware DES (Line 2), where the total allocated optical circuits can serve as a secondary fitness. Notably, this DES evaluation can also be accelerated by exploiting the isomorphism and independence of DP replicas to reduce the scale of the simulated task. Following standard crossover and mutation (Lines 7-8), the RepairTopo function (Alg. 6 in Appendix D) calibrates the child’s optical circuits to restore compliance with U and \bar{X} (Line 9). Unrepairable children are replaced by newly generated feasible configurations to maintain population diversity (Lines 10-11). The remaining steps follow a standard genetic algorithm framework to update the population and track the global optimal logical topology X^* . Collectively, Alg. 3 ensures an efficient convergence toward optimal, physically deployable logical topologies.

V. EVALUATIONS

In this section, we evaluate the performance of the proposed DAG-aware efficient logical topology optimization algorithm and compare it to existing solutions. All evaluations are conducted on a commodity computing platform equipped with an Intel i5-13500H (2.6 GHz) CPU and 32 GB of RAM.

A. Evaluation Setup

1) *Workloads*: We evaluate the logical topology optimization problem across four representative LLM training workloads (Megatron-177B, Mixtral-8X22B (MoE model), Megatron-462B, Deepseek-671B (MoE model)), with the evaluation configurations provided in Table I. The parallel strategy

Algorithm 3 SimBasedDomainAdaptedGA

Input: Active pod pairs E , port capacities $U = [U_1, \dots, U_{|P|}]$, upper bounds \bar{X} , GA parameters $(N_{\text{pop}}, N_{\text{gen}})$, \mathcal{M} , \mathcal{D}

Output: Logical topology X^*

- 1: $\mathcal{X} \leftarrow \{\text{FeasibleRandomInit}(E, U, \bar{X})\}_{i=1}^{N_{\text{pop}}}$
- 2: $\text{Fitness} \leftarrow \text{ParallelEvalDES}(\mathcal{X}, \mathcal{M}, \mathcal{D})$
- 3: $X^*, C_{\text{max}}^* \leftarrow \text{GetBestIndividual}(\mathcal{X}, \text{Fitness})$
- 4: **for** $gen = 1 \dots N_{\text{gen}}$ **do**
- 5: $\mathcal{X}_{\text{new}} \leftarrow \text{RetainElites}(\mathcal{X}, \text{Fitness})$
- 6: **while** $|\mathcal{X}_{\text{new}}| < N_{\text{pop}}$ **do**
- 7: $p_1, p_2 \leftarrow \text{TournamentSelection}(\mathcal{X}, \text{Fitness})$
- 8: $child \leftarrow \text{Mutate}(\text{Crossover}(p_1, p_2))$
- 9: $child, success \leftarrow \text{RepairTopo}(child, E, U, \bar{X})$
- 10: **if not** $success$ **then** $child \leftarrow \text{FeasibleRandomInit}(E, U, \bar{X})$
- 11: $\mathcal{X}_{\text{new}} \leftarrow \mathcal{X}_{\text{new}} \cup \{child\}$
- 12: **end while**
- 13: $\mathcal{X} \leftarrow \mathcal{X}_{\text{new}}; \text{Fitness} \leftarrow \text{ParallelEvalDES}(\mathcal{X}, \mathcal{M}, \mathcal{D})$
- 14: **if** $\min(\text{Fitness}) < C_{\text{max}}^*$ **then**
- 15: $X^*, C_{\text{max}}^* \leftarrow \text{GetBestIndividual}(\mathcal{X}, \text{Fitness})$
- 16: **end if**
- 17: **end for**
- 18: **return** X^*

configurations for these models are derived from the Megatron benchmarks [57–59]. To emulate practical scheduling strategies that increase the number of micro-batches to mitigate pipeline bubbles, the number of micro-batches processed per GPU per iteration is set to 8 times the PP size. The communication demand traces are generated via simAI [60, 61]. Furthermore, to simulate the fragmented model deployment typical of multi-tenant clusters, we limit the number of GPUs per Pod to 16 per DP replica for the two smaller models and 32 for the two larger models. Notably, allocating more GPUs per Pod per replica (i.e., # of GPUs / Pod / Replica) would localize more communication tasks within a single Pod, inadvertently simplifying the optimization problem. Therefore, we restrict this capacity to ensure sufficient inter-pod tasks, thereby rigorously evaluating the proposed algorithm’s performance. Specifically, we restrict inter-pod communication to PP and DP, as standard practice confines the latency-sensitive and bandwidth-intensive EP and TP to intra-pod electrical networks. Unless otherwise specified, the sequence length for LLM training is set to 4096, and inter-pod bandwidth is set to 400 Gb/s/GPU. For fairness, we assume that the maximum number of OCS ports (U_p) exclusively allocated to a training job in each Pod is strictly bounded by the number of GPUs assigned to that job within the Pod.

2) *Algorithms for Comparison*: Our evaluation includes six optimization algorithms: DELTA-Joint, DELTA-Topo, DELTA-Fast, and three traffic-matrix-based baselines: Prop-Alloc (derived from SiP-ML [43]), Sqrt-Alloc (a modified Prop-Alloc proposed in this work), and Iter-Halve (derived from TopoOpt [16]). Specifically, DELTA-Joint and DELTA-Topo construct the logical topology by solving the MILP formulated in Section III-B, with the former additionally

TABLE I: Evaluation configurations for the four representative LLMs.

Model Name	TP	PP	ETP	EP	# of GPUs	# of GPUs / Pod / Replica	# of Micro-batches
Megatron-177B	8	6	-	-	384	16	48
Mixtral-8X22B	2	8	1	8	128	16	64
Megatron-462B	8	16	-	-	1024	32	128
Deepseek-671B	2	16	1	8	256	32	128

co-optimizing the flow rates. DELTA-Fast is the heuristic algorithm detailed in Alg. 3. Regarding the baselines, Prop-Alloc treats all traffic demands as concurrent; to minimize the maximum transmission time, it mathematically corresponds to allocating links proportionally to the traffic volume. Sqrt-Alloc assumes that traffic demands originating from the same Pod to different destinations occur strictly sequentially (analogous to DP and PP communication within the same stage); accordingly, to minimize total transmission time, it allocates links in proportion to the square root of the traffic volume. Iter-Halve iteratively assigns a logical link to the communication pair with the highest weight—initially set by the traffic matrix—and subsequently halves that weight for the next round of allocation. Unless otherwise specified, the execution time for all algorithms is capped at 600s. The MILPs are solved using Gurobi 13.0. To maximize computational efficiency, our proposed DELTA suite employs four-thread parallelization.

3) *Performance Metric*: We adopt Normalized Communication Time (NCT) as the primary metric, defined as the ratio of the inter-pod communication time on the critical path under the OCS architecture to that under an ideal non-blocking electrical network with zero packet-processing delay. This normalization provides a standardized baseline for evaluating algorithms across diverse model architectures. Furthermore, focusing on the critical path captures the communication bottleneck that governs the actual iteration makespan.

B. Performance Comparison on Varying Inter-pod Bandwidths

Fig. 6 illustrates the NCT of the six evaluated algorithms under varying inter-pod bandwidth capacities. As inter-pod bandwidth increases, the communication-to-computation time ratio drops, shortening the relative duration of concurrent inter-pod communication for DP. This mitigates the communication degradation caused by allocating fewer logical links than the maximum number of concurrent flows, thereby reducing the NCT across all algorithms. While all algorithms benefit from this trend, the proposed DAG-driven DELTA suite consistently

outperforms traffic-matrix-based baselines. Specifically, across the four evaluated LLMs, DELTA-Joint achieves maximum NCT reductions of 11.5%, 13.7%, 10.7%, and 17.5% (at bandwidths of 800, 1600, 200, and 800 Gb/s, respectively) compared to the best-performing baselines. Generally, in next-generation network infrastructures with higher inter-pod bandwidths, the NCT reductions achieved by DELTA over the baselines become more substantial.

Within the DELTA suite, DELTA-Joint achieves the lowest NCT, confirming that topology and flow-rate co-optimization can further reduce the time in the critical path compared to topology-only methods. Across the four LLMs, it yields maximum NCT reductions of 11.5%, 10.6%, 10.7%, and 10.7% (at 800, 1600, 200, and 1600 Gb/s, respectively) over the topology-only DELTA. Moreover, DELTA-Fast performs identically to DELTA-Topo across all evaluated scenarios, validating the efficacy of the heuristic DELTA-Fast.

Notably, DELTA-Joint enables a static optical topology to achieve performance close to that of an ideal, non-blocking electrical switch (NCT = 1), without incurring the overhead of reconfigurations. Specifically, at an inter-pod bandwidth of 1600 Gb/s, DELTA-Joint reduces the performance gap to the theoretical ideal to 1.2%, 12.7%, 0%, and 0% across the four evaluated LLMs, respectively, demonstrating the power of DAG-aware joint optimization. We also note that at bandwidths of 400 Gb/s or below, communication performance under a static topology remains limited for workloads such as Megatron-177B, Mixtral-8X22B, and Deepseek-671B. However, this bottleneck can be effectively mitigated by reallocating surplus optical ports saved from other workloads (without compromising their original NCTs) to these bandwidth-bottlenecked workloads, as demonstrated in Section V-D.

Fig. 7 illustrates how DELTA-Joint approaches the performance of an ideal non-blocking electrical switch through its optimized flow-rate control strategy. As shown in the figure, when bandwidth contention is induced by concurrent communication from multiple stages, DELTA-Joint ensures that

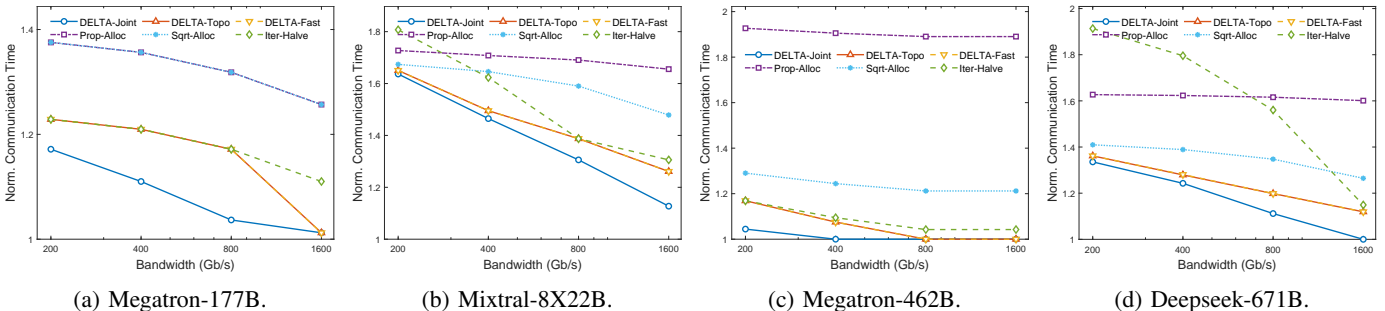


Fig. 6: Performance of DAG-driven vs. traffic-matrix-driven topology optimization under varying inter-pod bandwidths.

the critical flow (Stage 1), which dictates the global iteration makespan, continuously transmits at its physical upper bound of 200 GB/s (i.e., the aggregated injection bandwidth of 4 NICs). In contrast, the conventional fair-sharing strategy employed by DELTA-Topo causes this critical flow to experience a 25% rate degradation (from 200 to 150 GB/s) during contention periods.

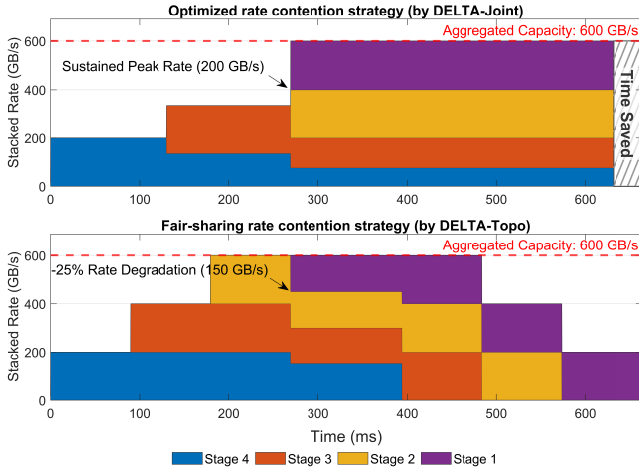


Fig. 7: Flow-rate control results of DP communication for Megatron-462B (400 Gb). For clarity, the time axis is zeroed at the moment Stage 4 initiates DP communication.

This sustained peak transmission in DELTA-Joint is achieved by exploiting the temporal slack of non-critical tasks. During contention periods, DELTA-Joint actively compresses the transmission rates of earlier-initiated flows (Stages 2 to 4) that possess temporal slack and dynamically reallocates the released bandwidth to Stage 1. Consequently, this flow-control strategy effectively prevents local congestion from delaying the critical task.

C. Performance Comparison on Varying Sequence Lengths

Beyond bandwidth, variations in model hyperparameters (e.g., sequence length) also reshape the communication bandwidth demands during LLM training. Consequently, we further investigate the performance of topology optimization algorithms on varying sequence lengths, as shown in Fig. 8.

As the sequence length increases, the DELTA suite not only consistently outperforms the baseline algorithms but

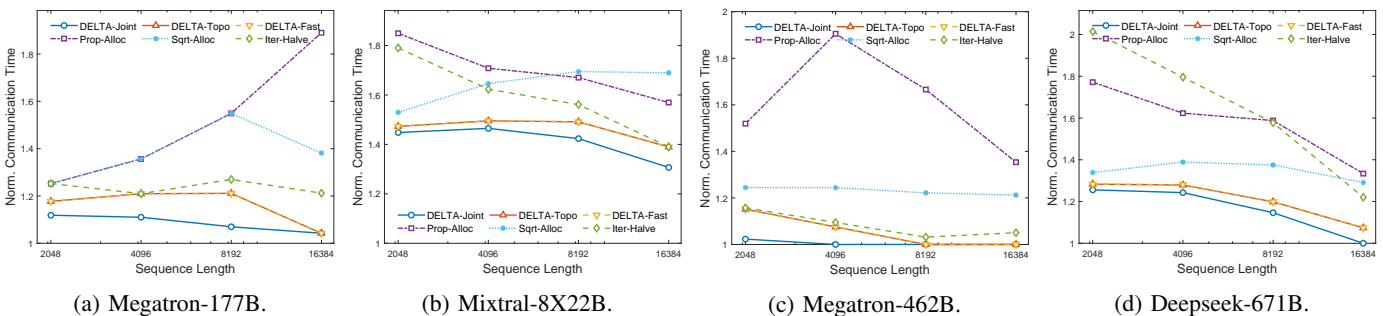
also exhibits a more consistent downward trend in NCT. Specifically, across the four evaluated LLMs, DELTA-Joint achieves maximum NCT reductions of 15.8%, 9.8%, 11.6%, and 18.1% (at sequence lengths of 8192, 4096, 2048, and 16384, respectively) compared to the best-performing baselines. Moreover, consistent with previous evaluations, DELTA-Fast retains its performance parity with DELTA-Topo. Fundamentally, an increase in sequence length triggers a twofold shift in the communication characteristics of LLM training: on the one hand, prolonged computation intervals (caused by the expanded sequence length) facilitate enhanced staggering of DP traffic, thereby creating better link time-multiplexing opportunities and mitigating concurrency bottlenecks; on the other hand, the concurrent “rectangular” bandwidth demands of PP scale proportionally with the sequence length. Leveraging the DAG-aware design, the DELTA suite more effectively navigates the dynamics of these superimposing effects.

Furthermore, when evaluated against an ideal non-blocking electrical network, DELTA-Joint exhibits a performance gap of 11.9%, 44.8%, 2.3%, and 25.6% across the four models at a sequence length of 2048. As the sequence scales to 16384, this gap narrows to 4.2%, 30.7%, 0%, and 0%, respectively. As the context window of large language models continues to expand, this performance disparity is projected to become increasingly marginal.

D. Reduction of Optical Port Consumption and Performance Gains via Port Reallocation

To enhance the performance of bandwidth-bottlenecked workloads, we minimize the total number of allocated optical ports by exploiting temporal slack in communication tasks along non-critical paths, thereby liberating port resources for reallocation. As illustrated in Fig. 9, this optimization reduces the allocated port ratio to below 80% (except for DELTA-Joint on Deepseek-671B at 81.3%) without prolonging the LLM training iteration time. The port reduction is most pronounced for the Megatron-462B model, which features a higher computation-to-communication ratio in its training; in this scenario, DELTA-Topo and DELTA-Joint further compress the port ratios to 68.8% and 60.9%, respectively.

Fig. 10 illustrates the reduced NCTs achieved by reallocating these recovered surplus ports to bandwidth-bottlenecked workloads. Specifically, Model^T is evaluated by deploying it with a reversed stage-to-Pod mapping relative to the original



(a) Megatron-177B.

(b) Mixtral-8X22B.

(c) Megatron-462B.

(d) Deepseek-671B.

Fig. 8: Performance of DAG-driven vs. traffic-matrix-driven topology optimization under varying sequence lengths.

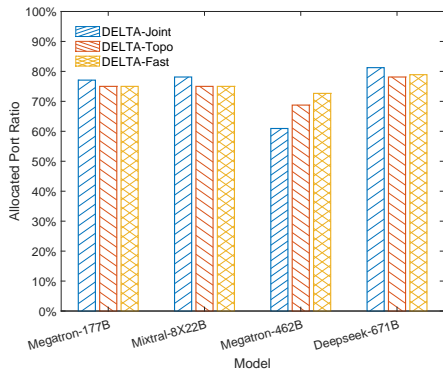


Fig. 9: Allocated port ratio compressed by DELTA variants (400 Gb/s, 4096 sequence length).

Model to absorb its released ports (serving as a controlled evaluation scheme to isolate performance gains from broader multi-tenant co-scheduling complexities that lie beyond the scope of this work). Benchmarked against an ideal non-blocking electrical switch operating at 400 Gb/s with a sequence length of 4096, this reallocation strategy significantly narrows the performance gaps for bandwidth-bottlenecked workloads. Specifically, the NCT overheads for Megatron-177B, Mixtral-8x22B, and Deepseek-671B are substantially reduced from 11.0% to 2.2%, 46.5% to 20.4%, and 24.3% to 2.8%, respectively. This degree of optimization is unattainable for conventional algorithms that construct the logical topology based solely on traffic matrices. Moreover, it highlights a promising strategy for multi-tenant AIDCs: when coupled with an appropriate job placement strategy, compressing the port allocation of bandwidth-insensitive workloads (e.g., Megatron-462B)—without inflating their iteration times—can be leveraged to provision bandwidth-bottlenecked workloads, thereby enabling otherwise severely constrained workloads to approach the performance of ideal non-blocking electrical networks. Notably, for Megatron-177B and Mixtral-8x22B, DELTA-Joint yields a slightly higher NCT than DELTA-Topo because it releases fewer ports to preserve its original optimal performance; we leave the investigation of these complex trade-offs to future work.

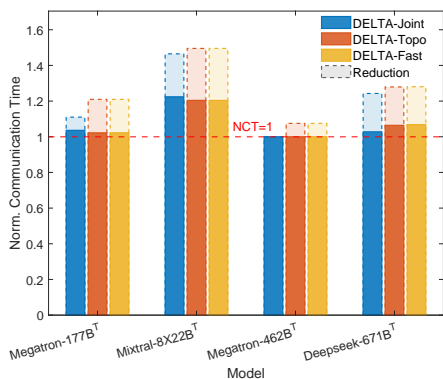


Fig. 10: Reduced NCTs of bandwidth-bottlenecked workloads by reallocating surplus ports (400 Gb/s, 4096 sequence length).

E. Execution Time Analysis

As detailed in Section IV-A, the algorithm’s computational complexity is dominated by the total number of inter-pod communication tasks, denoted as $|\mathcal{M}|$. The scale of $|\mathcal{M}|$ depends on two parameters: the PP size, which dictates the number of stages and proportionally scales both PP and DP task counts; and the number of micro-batches (hereafter, # of MBS), which scales the number of PP tasks linearly³. Since the configured PP size in Table I already reaches the recommended upper bound in the literature [57–59], and further scaling PP size is limited by pipeline bubble overheads, this evaluation isolates the impact of scaling the # of MBS on execution time.

Fig. 11 presents the execution times (including preprocessing time) of DELTA-Fast, DELTA-Topo, DELTA-Joint, and DELTA-Joint-HotStart under a varying # of MBS when optimizing topologies for Megatron-462B and Deepseek-671B. Notably, 512 is the maximum configuration reported in [58], whereas typical deployments adopt 128 or 256. Benefiting from the acceleration strategies in Section IV-B, DELTA-Fast’s execution time exhibits only marginal growth as the # of MBS increases. Across all evaluations, it converges to a stable state (where the optimal solution remains unchanged for 200 consecutive iterations) within tens of seconds. In contrast, the time required for DELTA-Topo and DELTA-Joint to converge to the final solution (defined as the point where, after stabilization, the objective gap between consecutive feasible solutions remains below 0.01%) increases significantly with the # of MBS. The maximum execution times for the two algorithms reach 896s and 928s for Megatron-462B, and 2020s and 1526s for Deepseek-671B, respectively. However, with the strategies in Section IV-A, the solving process can complete within 600s for a # of MBS up to 256. Crucially, the hot-start mechanism in DELTA-Joint-HotStart drastically reduces overall execution time (DELTA-Topo-HotStart is omitted since DELTA-Fast already yields a near-optimal solution). Specifically, hot starting reduces this time by an average of 50.4% (up to 69.6%) for Megatron-462B, and 72.7% (up to 89.5%) for Deepseek-671B, bringing the maximum execution times of DELTA-Joint-HotStart down to 358s and 637s for the two models, respectively. Given that these evaluations were performed on a consumer-grade laptop, the results strongly demonstrate the computational efficiency of the proposed algorithms.

VI. CONCLUSION

We propose DELTA, a computation-communication DAG-aware, efficient logical topology optimization framework for OCS-AIDCs. By encoding dynamic LLM training traffic features via DAG into the optimization model, alongside variable-length time interval MILP modeling, search space pruning, and heuristic acceleration, DELTA generates a high-quality logical topology within minutes. Furthermore, by exploiting temporal slack on non-critical communication tasks, DELTA can reallocate optical ports without compromising iteration time, effectively boosting bandwidth-bottlenecked workloads.

³Specifically, under the 1F1B scheduling scheme, after aggregating the communication tasks that concurrently start and finish at each stage, the number of PP tasks per model replica is $2 \times (\text{PP size} - 1) \times (\text{\# of MBS})$, while the number of DP tasks equals the PP size.

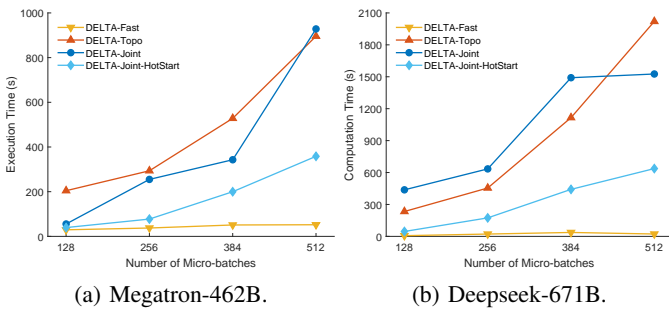


Fig. 11: Execution time of the algorithms in DELTA.

In multi-job scenarios, the disparate iteration cycles of various workloads cause their traffic overlaps to shift continuously, making accurate traffic prediction difficult. Moreover, since a single makespan objective cannot balance cluster throughput and fairness, a pragmatic solution to this complexity is to independently optimize the topology for each job using DELTA and aggregate these decisions via job-specific weights. Consequently, determining these weights to achieve data-center-level operational optimality constitutes a key direction for future research.

VII. ACKNOWLEDGEMENTS

This work was supported in part by the National Key Research and Development Project of China under Grant 2024YFB2908301 and in part by the National Natural Science Foundation of China (NSFC) under Grant 62331017. (Corresponding author: Weiqiang Sun.)

REFERENCES

- [1] J. Kaplan, S. McCandlish, T. Henighan, T. B. Brown, B. Chess, R. Child, S. Gray, A. Radford, J. Wu, and D. Amodei, *Scaling Laws for Neural Language Models*, 2020. arXiv: 2001.08361 [cs].
- [2] J. Hoffmann, S. Borgeaud, A. Mensch, E. Buchatskaya, T. Cai, E. Rutherford, D. d. L. Casas, L. A. Hendricks, J. Welbl, A. Clark, et al., *Training Compute-Optimal Large Language Models*, 2022. arXiv: 2203.15556 [cs].
- [3] Z. Zhang, C. Chang, H. Lin, Y. Wang, R. Arora, and X. Jin, "Is Network the Bottleneck of Distributed Training?" In *Proceedings of the Workshop on Network Meets AI & ML*, ser. NetAI '20, New York, NY, USA: Association for Computing Machinery, 2020, pp. 8–13.
- [4] E. Erdil and D. Schneider-Joseph, *Data movement limits to frontier model training*, 2024. arXiv: 2411.01137 [cs].
- [5] A. Gholami, Z. Yao, S. Kim, C. Hooper, M. W. Mahoney, and K. Keutzer, "AI and Memory Wall," *IEEE Micro*, vol. 44, no. 3, pp. 33–39, 2024, ISSN: 1937-4143.
- [6] K. Benyahya, A. G. Diaz, J. Liu, V. Lyutsarev, M. Pantouvaki, K. Shi, S. Y. Siew, H. Ballani, T. Burrigge, D. Cletheroe, et al., "Mosaic: Breaking the Optics versus Copper Trade-off with a Wide-and-Slow Architecture and MicroLEDs," in *Proceedings of the ACM SIGCOMM 2025 Conference*, ser. SIGCOMM '25, New York, NY, USA: Association for Computing Machinery, 2025, pp. 234–247.
- [7] Y. Wei, T. Hu, C. Liang, and Y. Cui, "Communication Optimization for Distributed Training: Architecture, Advances, and Opportunities," *IEEE Network*, vol. 39, no. 3, pp. 241–248, 2025, ISSN: 1558-156X.
- [8] K. Qian, Y. Xi, J. Cao, J. Gao, Y. Xu, Y. Guan, B. Fu, X. Shi, F. Zhu, R. Miao, et al., "Alibaba HPN: A Data Center Network for Large Language Model Training," in *Proceedings of the ACM SIGCOMM 2024 Conference*, ser. ACM SIGCOMM '24, New York, NY, USA: Association for Computing Machinery, 2024, pp. 691–706.
- [9] W. Tian, H. Hou, H. Dang, X. Cao, D. Li, S. Chen, and B. Ma, "Progress in Research on Co-Packaged Optics," *Micromachines*, vol. 15, no. 10, p. 1211, 2024, ISSN: 2072-666X.
- [10] Brad Smith, *A New Era in Data Center Networking with NVIDIA Silicon Photonics-based Network Switching*, 2025.
- [11] Ashkan Seyedi, *Scaling AI Factories with Co-Packaged Optics for Better Power Efficiency*, 2025.
- [12] E. Ding, C. Ouyang, and R. Singh, "Photonic Rails in ML Datacenters," in *Proceedings of the 24th ACM Workshop on Hot Topics in Networks*, ser. HotNets '25, New York, NY, USA: Association for Computing Machinery, 2025, pp. 149–159.
- [13] L. Poutievski, O. Mashayekhi, J. Ong, A. Singh, M. Tariq, R. Wang, J. Zhang, V. Beauregard, P. Conner, S. Gribble, et al., "Jupiter evolving: Transforming google's datacenter network via optical circuit switches and software-defined networking," in *Proceedings of the ACM SIGCOMM 2022 Conference*, ser. SIGCOMM '22, New York, NY, USA: Association for Computing Machinery, 2022, pp. 66–85.
- [14] R. Urata, H. Liu, K. Yasumura, E. Mao, J. Berger, X. Zhou, C. Lam, R. Bannon, D. Hutchinson, D. Nelson, et al., *Mission Apollo: Landing Optical Circuit Switching at Datacenter Scale*, 2022. arXiv: 2208.10041.
- [15] H. Liu, R. Urata, K. Yasumura, X. Zhou, R. Bannon, J. Berger, P. Dashti, N. Jouppi, C. Lam, S. Li, et al., "Lightwave Fabrics: At-Scale Optical Circuit Switching for Datacenter and Machine Learning Systems," in *Proceedings of the ACM SIGCOMM 2023 Conference*, New York NY USA: ACM, 2023, pp. 499–515.
- [16] W. Wang, M. Khazraee, Z. Zhong, M. Ghobadi, Z. Jia, D. Mudigere, Y. Zhang, and A. Kewitsch, "TopoOpt: Co-optimizing Network Topology and Parallelization Strategy for Distributed Training Jobs," in *20th USENIX Symposium on Networked Systems Design and Implementation, NSDI 2023, Boston, MA, April 17-19, 2023*, M. Balakrishnan and M. Ghobadi, Eds., USENIX Association, 2023, pp. 739–767. arXiv: 2202.00433.
- [17] N. Jouppi, G. Kurian, S. Li, P. Ma, R. Nagarajan, L. Nai, N. Patil, S. Subramanian, A. Swing, B. Towles, et al., "TPU v4: An Optically Reconfigurable Supercomputer for Machine Learning with Hardware Support for Embeddings," in *Proceedings of the 50th Annual International Symposium on Computer Architecture*, ser. ISCA '23, New York, NY, USA: Association for Computing Machinery, 17, 2023, pp. 1–14.
- [18] Y. Zu, A. Ghaffarkhah, H.-V. Dang, B. Towles, S. Hand, S. Huda, A. Bello, A. Kolbasov, A. Rezaei, D. Du, et al., "Resiliency at Scale: Managing Google's TPUv4 Machine Learning Supercomputer," in *21st USENIX Symposium on Networked Systems Design and Implementation (NSDI 24)*, 2024, pp. 761–774.
- [19] X. Liao, Y. Sun, H. Tian, X. Wan, Y. Jin, Z. Wang, Z. Ren, X. Huang, W. Li, K. F. Tse, et al., "MixNet: A Runtime Reconfigurable Optical-Electrical Fabric for Distributed Mixture-of-Experts Training," in *Proceedings of the ACM SIGCOMM 2025 Conference*, ser. SIGCOMM '25, New York, NY, USA: Association for Computing Machinery, 2025, pp. 554–574.
- [20] J. Zerwas, W. Kellerer, and A. Blenk, "What You Need to Know About Optical Circuit Reconfigurations in Datacenter Networks," in *2021 33th International Teletraffic Congress (ITC-33)*, 2021, pp. 1–9.
- [21] M. Zhang, J. Zhang, R. Wang, R. Govindan, J. C. Mogul, and A. Vahdat, *Gemini: Practical Reconfigurable Datacenter Networks with Topology and Traffic Engineering*, 2021. arXiv: 2110.08374 [cs].
- [22] Nvidia, B. Adler, N. Agarwal, A. Aithal, D. H. Anh, P. Bhattacharya, A. Brundyn, J. Casper, B. Catanzaro, S. Clay, et al., *Nemotron-4 340B Technical Report*, 2024. arXiv: 2406.11704 [cs].
- [23] Z. Jiang, H. Lin, Y. Zhong, Q. Huang, Y. Chen, Z. Zhang, Y. Peng, X. Li, C. Xie, S. Nong, et al., "MegaScale: Scaling Large Language Model Training to More Than 10,000 GPUs," in *21st USENIX Symposium on Networked Systems Design and Implementation (NSDI 24)*, 2024, pp. 745–760.
- [24] C. Jin, Z. Jiang, Z. Bai, Z. Zhong, J. Liu, X. Li, N. Zheng, X. Wang, C. Xie, Q. Huang, et al., *MegaScale-MoE: Large-Scale Communication-Efficient Training of Mixture-of-Experts Models in Production*, 2025. arXiv: 2505.11432 [cs].
- [25] W. Feng, Y. Chen, S. Wang, Y. Peng, H. Lin, and M. Yu, "Optimus: Accelerating large-scale multi-modal LLM training by bubble exploitation," in *Proceedings of the 2025 USENIX Conference on Usenix Annual Technical Conference*, ser. USENIX ATC '25, USA: USENIX Association, 2025, pp. 161–177.
- [26] M. Liang, H. T. Kassa, W. Fu, B. Coutinho, L. Feng, and C. Delimitrou, "Lumos: Efficient performance modeling and estimation for large-scale LLM training," in *Proceedings of Machine Learning and Systems*, M. Zaharia, G. Joshi, and Y. Lin, Eds., vol. 7, MLSys, 2025.
- [27] S. Zhao, P. Cao, and X. Wang, "Understanding the Performance Guarantee of Physical Topology Design for Optical Circuit Switched Data Centers," *Proc. ACM Meas. Anal. Comput. Syst.*, vol. 5, no. 3, 42:1–42:24, 2021.

- [28] X. Han, Y. Lv, W. Jiang, S. Zhang, Y. Mao, S. Zhao, Z. Liu, Z. Liu, P. Cao, X. Liu, et al., *A Highly Scalable LLM Clusters with Optical Interconnect*, 2025. arXiv: 2411.01503 [cs].
- [29] M. Y. Teh, S. Zhao, and K. Bergman, *METTEOR: Robust Multi-Traffic Topology Engineering for Commercial Data Center Networks*, 2020. arXiv: 2002.00473 [cs].
- [30] P. Cao, S. Zhao, M. Y. The, Y. Liu, and X. Wang, “TROD: Evolving From Electrical Data Center to Optical Data Center,” in *2021 IEEE 29th International Conference on Network Protocols (ICNP)*, 2021, pp. 1–11.
- [31] M. Y. Teh, S. Zhao, P. Cao, and K. Bergman, “Enabling Quasi-Static Reconfigurable Networks With Robust Topology Engineering,” *IEEE/ACM Transactions on Networking*, vol. 31, no. 3, pp. 1056–1070, 2023, ISSN: 1558-2566.
- [32] S. Zhao, R. Wang, J. Zhou, J. Ong, J. C. Mogul, and A. Vahdat, “Minimal Rewiring: Efficient Live Expansion for Clos Data Center Networks,” in *16th USENIX Symposium on Networked Systems Design and Implementation (NSDI 19)*, 2019, pp. 221–234.
- [33] K. Hanauer, M. Henzinger, S. Schmid, and J. Trummer, “Fast and Heavy Disjoint Weighted Matchings for Demand-Aware Datacenter Topologies,” in *IEEE INFOCOM 2022 - IEEE Conference on Computer Communications*, 2022, pp. 1649–1658.
- [34] K. Hanauer, M. Henzinger, L. Ost, and S. Schmid, “Dynamic Demand-Aware Link Scheduling for Reconfigurable Datacenters,” in *IEEE INFOCOM 2023 - IEEE Conference on Computer Communications*, 2023, pp. 1–10.
- [35] J. Wang, G. Zhao, H. Xu, and H. Wang, “Leaf: Improving QoS for Reconfigurable Datacenters with Multiple Optical Circuit Switches,” in *2024 IEEE/ACM 32nd International Symposium on Quality of Service (IWQoS)*, 2024, pp. 1–10.
- [36] L. Liu, H. Yu, G. Sun, H. Zhou, Z. Li, and S. Luo, “Online job scheduling for distributed machine learning in optical circuit switch networks,” *Knowledge-Based Systems*, vol. 201–202, p. 106002, 2020, ISSN: 0950-7051.
- [37] C. Wang, N. Yoshikane, F. Balasis, and T. Tsuritani, “OSDL: Dedicated optical slice provisioning in support of distributed deep learning,” *Computer Networks*, vol. 214, p. 109191, 2022, ISSN: 1389-1286.
- [38] X. Dong, H. Yang, Y. Zhang, X. Xie, and Z. Zhu, “On Scheduling DML Jobs in All-Optical DCNs with In-Network Computing,” in *GLOBECOM 2024 - 2024 IEEE Global Communications Conference*, 2024, pp. 5090–5095.
- [39] X. Xie, B. Tang, X. Chen, and Z. Zhu, “P4INC-AOI: All-Optical Interconnect Empowered by In-Network Computing for DML Workloads,” *IEEE Transactions on Networking*, pp. 1–16, 2025, ISSN: 2998-4157.
- [40] L. Liu, X. Xu, P. Zhou, X. Chen, D. Ergu, H. Yu, G. Sun, and M. Guizani, “PSScheduler: A parameter synchronization scheduling algorithm for distributed machine learning in reconfigurable optical networks,” *Neurocomputing*, vol. 616, p. 128876, 2025, ISSN: 0925-2312.
- [41] C. Shou, G. Liu, H. Nie, H. Meng, Y. Zhou, Y. Jiang, W. Lv, Y. Xu, Y. Lu, Z. Chen, et al., “InfiniteHBD: Building Datacenter-Scale High-Bandwidth Domain for LLM with Optical Circuit Switching Transceivers,” in *Proceedings of the ACM SIGCOMM 2025 Conference*, ser. SIGCOMM ’25, New York, NY, USA: Association for Computing Machinery, 2025, pp. 1–23.
- [42] V. Addanki, “When Light Bends to the Collective Will: A Theory and Vision for Adaptive Photonic Scale-up Domains,” in *Proceedings of the 24th ACM Workshop on Hot Topics in Networks*, ser. HotNets ’25, New York, NY, USA: Association for Computing Machinery, 2025, pp. 326–334.
- [43] M. Khani, M. Ghobadi, M. Alizadeh, Z. Zhu, M. Glick, K. Bergman, A. Vahdat, B. Klenk, and E. Ebrahimi, “SiP-ML: High-bandwidth optical network interconnects for machine learning training,” in *Proceedings of the 2021 ACM SIGCOMM 2021 Conference*, ser. SIGCOMM ’21, New York, NY, USA: Association for Computing Machinery, 2021, pp. 657–675.
- [44] S. H. Hashemi, S. Abdu Jyothi, and R. Campbell, “TicTac: Accelerating Distributed Deep Learning with Communication Scheduling,” *Proceedings of Machine Learning and Systems*, vol. 1, pp. 418–430, 2019.
- [45] A. Jayarajan, J. Wei, G. Gibson, A. Fedorova, and G. Pekhimenko, “Priority-based Parameter Propagation for Distributed DNN Training,” *Proceedings of Machine Learning and Systems*, vol. 1, pp. 132–145, 2019.
- [46] Y. Peng, Y. Zhu, Y. Chen, Y. Bao, B. Yi, C. Lan, C. Wu, and C. Guo, “A generic communication scheduler for distributed DNN training acceleration,” in *Proceedings of the 27th ACM Symposium on Operating Systems Principles*, ser. SOSP ’19, New York, NY, USA: Association for Computing Machinery, 2019, pp. 16–29.
- [47] Y. Bao, Y. Peng, Y. Chen, and C. Wu, “Preemptive All-reduce Scheduling for Expediting Distributed DNN Training,” in *IEEE INFOCOM 2020 - IEEE Conference on Computer Communications*, 2020, pp. 626–635.
- [48] F. Li, S. Zhao, Y. Qing, X. Chen, X. Guan, S. Wang, G. Zhang, and H. Cui, “Fold3D: Rethinking and Parallelizing Computational and Communicational Tasks in the Training of Large DNN Models,” *IEEE Transactions on Parallel and Distributed Systems*, vol. 34, no. 5, pp. 1432–1449, 2023, ISSN: 1558-2183.
- [49] S. Li, K. Lu, Z. Lai, W. Liu, K. Ge, and D. Li, “A Multidimensional Communication Scheduling Method for Hybrid Parallel DNN Training,” *IEEE Transactions on Parallel and Distributed Systems*, vol. 35, no. 8, pp. 1415–1428, 2024, ISSN: 1558-2183.
- [50] S. Kandula, I. Menache, R. Schwartz, and S. R. Babbula, “Calendar for wide area networks,” in *Proceedings of the 2014 ACM Conference on SIGCOMM*, ser. SIGCOMM ’14, New York, NY, USA: Association for Computing Machinery, 2014, pp. 515–526.
- [51] S. H. Mohamed, A. Hammadi, T. E. H. El-Gorashi, and J. M. H. Elmoghani, *Optimizing Co-flows Scheduling and Routing in Data Centre Networks for Big Data Applications*, 2020. arXiv: 2008.03497 [cs].
- [52] J. Li, W. Shi, N. Zhang, and X. Shen, “Delay-Aware VNF Scheduling: A Reinforcement Learning Approach With Variable Action Set,” *IEEE Transactions on Cognitive Communications and Networking*, vol. 7, no. 1, pp. 304–318, 2021, ISSN: 2332-7731.
- [53] B. Fatemipour, W. Shi, and M. St-Hilaire, “A Cost-Effective and Multi-Source-Aware Replica Migration Approach for Geo-Distributed Data Centers,” in *2022 IEEE Cloud Summit*, 2022, pp. 17–22.
- [54] T. Wang, S. Chen, Y. Zhu, A. Tang, and X. Wang, “LinkSlice: Fine-Grained Network Slice Enforcement Based on Deep Reinforcement Learning,” *IEEE Journal on Selected Areas in Communications*, vol. 40, no. 8, pp. 2378–2394, 2022, ISSN: 1558-0008.
- [55] N. Diaz and N. Gautam, “Non-Periodic Traffic Allocation in Time-Aware TSN Networks,” *IEEE Access*, vol. 13, pp. 187758–187773, 2025, ISSN: 2169-3536.
- [56] L. A. Wolsey, *Integer Programming*. John Wiley & Sons, 2020.
- [57] D. Liu, Z. Yan, X. Yao, T. Liu, V. Korthikanti, E. Wu, S. Fan, G. Deng, H. Bai, J. Chang, et al., *MoE Parallel Folding: Heterogeneous Parallelism Mappings for Efficient Large-Scale MoE Model Training with Megatron Core*, 2025. arXiv: 2504.14960 [cs].
- [58] NVIDIA Corporation, *Performance Summary — NeMo Megatron-Bridge 0.2.0 documentation*, 2025.
- [59] NVIDIA Corporation, *Megatron-LM and Megatron Core*, 2026.
- [60] X. Li, H. Zhou, Q. Li, S. Zhang, and G. Lu, “AICB: A benchmark for evaluating the communication subsystem of LLM training clusters,” *BenchCouncil Transactions on Benchmarks, Standards and Evaluations*, vol. 5, no. 1, p. 100212, 2025, ISSN: 27724859.
- [61] X. Wang, Q. Li, Y. Xu, G. Lu, D. Li, L. Chen, H. Zhou, L. Zheng, S. Zhang, Y. Zhu, et al., “SimAI: Unifying Architecture Design and Performance Tuning for Large-Scale Large Language Model Training with Scalability and Precision,” in *22nd USENIX Symposium on Networked Systems Design and Implementation (NSDI 25)*, 2025, pp. 541–558.

APPENDIX A

MILP FORMULATION WITH FIXED-TIME-STEP FOR LOGICAL TOPOLOGY OPTIMIZATION

Serving as a comparative baseline for the variable-length time interval MILP formulation, this appendix details the fixed-time-step counterpart, which formulates the topology optimization problem by discretizing the time horizon into uniform slices.

Temporal Discretization:

The considered time horizon is partitioned into a set of fixed-duration time slices, indexed by $\mathcal{T} = \{1, 2, \dots, T\}$, where the integer T denotes the total number of slices and each slice has a constant length Δt .

Decision Variables:

- $r_{m,t}$: A continuous variable denoting the instantaneous transmission rate of task m during time slice t .
- $y_{m,t}$: A binary variable indicating whether task m is active during time slice t .

- $S_{m,t}, C_{m,t}$: Binary auxiliary variables indicating the initiation and completion of task m at time slice t .
- $u_{i,j,t}$: A continuous auxiliary variable denoting the normalized fair-share reference rate across the aggregated optical circuits between Pod i and Pod j during time slice t . It facilitates the fair distribution (optional) of aggregated bandwidth across all active tasks sharing this inter-pod connection.
- $x_{i,j}$: An integer variable denoting the number of optical circuits/ports allocated between Pod i and Pod j .

Unless otherwise specified, all indices i, j range over the set of \mathcal{P} , g ranges over the set of \mathcal{G} , t ranges over the set of \mathcal{T} , and m belongs to the set of \mathcal{M} .

Objectives:

The primary optimization objective is to minimize the iteration time of the training task:

$$\min C. \quad (19)$$

A secondary objective minimizes total optical port consumption without increasing the optimal makespan C^* :

$$\min \sum_{i \in \mathcal{P}} \sum_{j \in \mathcal{P}, j \neq i} x_{i,j}, \quad \text{s.t. } C \leq C^*. \quad (20)$$

Constraints:

1) Topology-Related Constraints:

$$\begin{cases} \sum_{j \in \mathcal{P}, j \neq i} x_{i,j} \leq U_i, & \forall i. \\ \sum_{i \in \mathcal{P}, i \neq j} x_{i,j} \leq U_j, & \forall j. \\ x_{i,j} = x_{j,i}, & \forall i, j. \end{cases} \quad (21)$$

Eq. (21) defines the physical port limits and bidirectional symmetry, following the same logic as the main text.

2) Optical Circuit and NIC Capacity-Related Constraints:

$$\sum_{m \in \mathcal{M}(i,j)} r_{m,t} \leq x_{i,j} \cdot B, \quad \forall t, \forall i, j. \quad (22)$$

$$\begin{cases} \sum_{m \in \Phi_{\text{src}}(g)} \frac{r_{m,t}}{F_m} \leq B, & \forall t, g. \\ \sum_{m \in \Phi_{\text{dst}}(g)} \frac{r_{m,t}}{F_m} \leq B, & \forall t, g. \end{cases} \quad (23)$$

Eq. (22) and (23) bound the aggregated rates by the allocated logical link bandwidth and individual NIC injection/reception capacities, respectively.

3) Task Lifecycle and Data Transmission Constraints:

$$\sum_t S_{m,t} = 1, \quad \sum_t C_{m,t} = 1, \quad \forall m. \quad (24)$$

$$y_{m,t} - y_{m,t-1} = S_{m,t} - C_{m,t}, \quad \forall m, t. \quad (25)$$

$$\sum_{t=1}^T (r_{m,t} \cdot \Delta t) \geq V_m, \quad \forall m. \quad (26)$$

$$r_{m,t} \leq y_{m,t} \cdot (F_m \cdot B), \quad \forall m, t. \quad (27)$$

Eq. (24) and (25) enforce unique initiation and completion points, maintaining state continuity throughout the lifecycle of each task. Eq. (26) guarantees that the cumulative data volume transmitted satisfies the predefined demand V_m . Furthermore,

Eq. (27) explicitly couples the continuous transmission rate with the binary state, ensuring that transmission only occurs during active intervals ($y_{m,t} = 1$) while respecting the flow-level physical bandwidth limits.

4) Inter-Pod Communication DAG Constraints:

$$\sum_t (t \cdot S_{m,t}) \geq \sum_t (t \cdot C_{m_{\text{pre}},t}) + \left\lceil \frac{\delta_{m_{\text{pre}} \rightarrow m}}{\Delta t} \right\rceil, \quad (28)$$

$$\forall (m_{\text{pre}}, m, \delta) \in \mathcal{D}.$$

Eq. (28) guarantees that task execution strictly adheres to the precedence requirements defined in the reduced DAG \mathcal{D} .

5) Flow Fairness Constraints (Optional for Comparison):

$$-M(1 - y_{m,t}) \leq \frac{r_{m,t}}{F_m} - u_{i,j,t} \leq M(1 - y_{m,t}), \quad (29)$$

$$\forall t, (i, j), m \in \mathcal{M}(i, j).$$

Eq. (29) uses the Big-M method to simulate conventional fair-sharing mechanisms by equalizing the normalized rates of concurrent flows on the same link.

6) Objective Function Constraint:

$$C \geq t \cdot C_{m,t}, \quad \forall m, t. \quad (30)$$

Eq. (30) defines the global completion time as the envelope of all individual task completion times.

APPENDIX B

LIMITATIONS OF TOPOLOGY-SORTING-BASED SEARCH SPACE PRUNING

Relying exclusively on topological sorting for search space pruning is conservative. First, when two tasks (e.g., the B3S2 PPFwd and B1S3 PPBwd nodes in Fig. 3b) share the same topological order on \mathcal{D} but exhibit different time intervals δ relative to their predecessors, the task subject to a longer delay should logically be activated in a later time interval. However, because its earliest active index remains identical to that of the earlier task, topological sorting yields lower-bound (left-side) index redundancy (as shown by the left boundary of the feasible region for the fourth task in Fig. 5b).

Second, consider a task serving as a common predecessor across multiple dependency branches (e.g., the B4S3 PPBwd node in Fig. 3b, which is a prerequisite for three different DP communication tasks). If its multiple successors have varying startup interval requirements, this predecessor should logically complete earlier to accommodate their distinct active intervals. Yet, when determining its latest active index, topological sorting adopts the pessimistic assumption that all successors might start and stop simultaneously (i.e., collectively occupying only a single time interval). This oversimplification generates upper-bound (right-side) index redundancy (as demonstrated by the right boundary of the feasible region for the fourth-to-last task in Fig. 5b).

APPENDIX C

SUPPLEMENTARY ALGORITHMS FOR SEARCH SPACE PRUNING

This appendix details the Alg. 4 (CalTaskTimeWindows) utilized in Alg. 1. Alg. 4 computes the Earliest Start Time

(EST) and Latest Completion Time (LCT) for each task $m \in \mathcal{M}$. The algorithm operates in three steps. First, it initializes the minimum physical duration τ_m based on the task data volume V_m and per-flow bandwidth B (Line 2). Second, a forward propagation traversal over the reduced computation-communication DAG \mathcal{D} calculates the EST for each task by respecting all rigid dependency intervals δ (Line 6-13). Finally, backward propagation starting from the coarsely estimated upper bound on the iteration time \hat{T}_{up} yields the LCT (Lines 14-21). The effect of Alg. 4 is illustrated in Fig. 12.

Algorithm 4 CalTaskTimeWindows

Input: \mathcal{M} , \mathcal{D} , Bandwidth B , Time upper bound \hat{T}_{up} .
Output: EST, LCT.

▷ **Step 1: Initialization & Minimum Duration Estimation**

```

1: for each  $m \in \mathcal{M}$  do
2:    $\tau_m \leftarrow V_m / (F_m \cdot B)$  ▷ Minimum physical duration
3:    $EST_m \leftarrow 0$ ,  $LCT_m \leftarrow \hat{T}_{up}$ 
4:   Compute in-degree  $deg_{in}(m)$  and out-degree  $deg_{out}(m)$  based on  $\mathcal{D}$ .
5: end for
    
```

▷ **Step 2: Forward Propagation (Earliest Start Time)**

```

6:  $\mathcal{Q} \leftarrow \{m \in \mathcal{M} \mid deg_{in}(m) = 0\}$ 
7: while  $\mathcal{Q} \neq \emptyset$  do
8:    $u \leftarrow \mathcal{Q}.pop()$ 
9:   for each dependency  $(u, v, \delta) \in \mathcal{D}$  do
10:     $EST_v \leftarrow \max(EST_v, EST_u + \tau_u + \delta)$ 
11:     $deg_{in}(v) \leftarrow deg_{in}(v) - 1$ ; if  $deg_{in}(v) == 0$  then
     $\mathcal{Q}.push(v)$ 
12:   end for
13: end while
    
```

▷ **Step 3: Backward Propagation (Latest Completion Time)**

```

14:  $\mathcal{Q} \leftarrow \{m \in \mathcal{M} \mid deg_{out}(m) = 0\}$ 
15: while  $\mathcal{Q} \neq \emptyset$  do
16:    $v \leftarrow \mathcal{Q}.pop()$ 
17:   for each dependency  $(u, v, \delta) \in \mathcal{D}$  do
18:     $LCT_u \leftarrow \min(LCT_u, LCT_v - \tau_v - \delta)$ 
19:     $deg_{out}(u) \leftarrow deg_{out}(u) - 1$ ; if  $deg_{out}(u) == 0$  then
     $\mathcal{Q}.push(u)$ 
20:   end for
21: end while
22: return EST, LCT =  $\{EST_m, LCT_m \mid m \in \mathcal{M}\}$ 
    
```

Note that Fig. 12 and Fig. 5b exhibit similarly compact profiles, suggesting that an analogous approach could be employed to prune the search space for fixed-time-step MILP formulation. However, in our empirical evaluations, even with a relatively coarse time resolution of 0.1 ms (compared to the millisecond-level duration of a single PP communication) and similar search space pruning techniques, solving the fixed-time-step MILP corresponding to a slightly large-scale problem still required tens of hours.

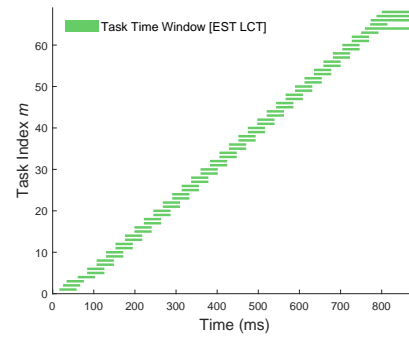


Fig. 12: DAG-aware task time window estimation for search space pruning (LLM training setup as in Fig. 5).

APPENDIX D
 SUBROUTINES FOR DOMAIN-ADAPTED GENETIC
 ALGORITHM

This appendix details the initialization and repair subroutines used in Alg. 3 of the domain-adapted genetic algorithm. Alg. 5 (FeasibleRandomInit) constructs a valid initial logical topology X that adheres to both the physical port capacities U and the upper bounds \bar{X} . First, it initializes the current port usage and calculates the unprocessed degrees for all pods to anticipate future connectivity requirements (Lines 1-2). Second, it iteratively processes each active pod pair $e \in E$ to determine the maximum allowable capacity by reserving ports for remaining connections and bounding it with \bar{X}_e (Lines 3-10). Finally, it uniformly samples a valid link capacity x_e within the calculated limits and updates the physical port usage for the corresponding endpoints (Lines 11-15).

Algorithm 5 FeasibleRandomInit

Input: Active pod pairs (edges) E , port capacities $U = [U_1, \dots, U_{|P|}]$, upper bounds \bar{X}

Output: A feasible logical topology X

```

1: Initialize port usage  $U_p^{used} \leftarrow 0$  for all  $p \in \mathcal{P}$ 
▷ Initialize unprocessed degrees for future lookahead
2: Let  $D_p \leftarrow |\{e \in E \mid e \text{ connects to } p\}|$  for all  $p \in \mathcal{P}$ 
3: for each edge  $e = (u, v) \in E$  do
4:   ▷ Update future degrees (remaining ports after current e)
5:    $D_u \leftarrow D_u - 1$ ;  $D_v \leftarrow D_v - 1$ 
6:   ▷ Calculate remaining valid ports
7:    $R_u \leftarrow U_u - U_u^{used}$ ;  $R_v \leftarrow U_v - U_v^{used}$ 
8:   ▷ Reserve ports for future connectivity
9:    $R'_u \leftarrow R_u - D_u$ ;  $R'_v \leftarrow R_v - D_v$ 
10:  ▷ Determine maximum allowable capacity and bound it
11:   $limit \leftarrow \min(R'_u, R'_v, \bar{X}_e)$ 
12:   $limit \leftarrow \max(1, limit)$  ▷ Ensure basic connectivity
13:  ▷ Sample capacity and update usage
14:   $x_e \sim \mathcal{U}\{1, limit\}$ 
15:   $U_u^{used} \leftarrow U_u^{used} + x_e$ ;  $U_v^{used} \leftarrow U_v^{used} + x_e$ 
16: end for
17: return  $X = \{x_e \mid e \in E\}$ 
    
```

To address invalid offspring generated during crossover and mutation, Alg. 6 (RepairTopo) restores compliance with all physical and logical constraints. First, a base trimming process enforces the capacity upper bounds \bar{X}_e and ensures connectivity for each active pod pair (Lines 1-3). Second, a port overflow reduction mechanism identifies overloaded pods and randomly decrements the capacity of their reducible edges until the physical port limits are met or no reducible edges remain (Lines 4-15). Finally, a verification step checks whether all port constraints U_p are globally satisfied, returning the repaired topology and a boolean success flag (Lines 16-20).

Algorithm 6 RepairTopo

Input: Mutant/Crossover topology X' , active pod pairs E , port capacities $U = [U_1, \dots, U_{|\mathcal{P}|}]$, upper bounds \bar{X}

Output: Repaired topology X' , boolean flag *success* indicating repair status

▷ **Step 1: Base Trimming**

1: **for each** $e \in E$ **do**
 2: $x'_e \leftarrow \max(1, \min(x'_e, \bar{X}_e))$ ▷ Enforce bounds & connectivity
 3: **end for**

▷ **Step 2: Port Overflow Reduction**

4: Compute current port usage U_p^{used} for all $p \in \mathcal{P}$
 5: **while** $\exists p \in \mathcal{P}$ such that $U_p^{\text{used}} > U_p$ **do**
 6: Let $\mathcal{P}_{\text{over}}$ be the set of overloaded pods
 7: Randomly select a pod $p \in \mathcal{P}_{\text{over}}$
 8: $E_p \leftarrow \{e \in E \mid e \text{ connects to } p \text{ and } x'_e > 1\}$
 9: **if** $E_p = \emptyset$ **then**
 10: **break** ▷ Repair failed: overloaded but no reducible edges
 11: **end if**
 12: Randomly select a reducible edge $e \in E_p$
 13: $x'_e \leftarrow x'_e - 1$
 14: Update U^{used} locally for the endpoints of e
 15: **end while**

▷ **Step 3: Final Verification**

16: **if** all $U_p^{\text{used}} \leq U_p$ **for** $p \in \mathcal{P}$ **then**
 17: **return** X' , True
 18: **else**
 19: **return** X' , False
 20: **end if**
